Singularity Conditions for Continuum Parallel Robots

Sébastien Briot, Alexandre Goldsztejn

Singularity Conditions for Continuum Parallel Robots

Sébastien Briot[1] and Alexandre Goldsztejn[1]

***Abstract*—Research on continuum parallel robots has been essentially devoted to the computation of their geometrico-static models and of their performance in terms of workspace size, accuracy, compliance, force transmission and manipulability. Their singularity analysis has been limited to the identification of a limited number of singular configurations, without any deep investigation of the physical phenomena occuring in these singularities.**

In this paper, we define the singularity conditions for continuum parallel robots. We provide a straightforward interpretation of the phenomena occurring in singularities. Especially, we prove that some singularities appear when the robot potential energy has a local isovalue. Because of this property, we show that these singularities separate the stable configurations from the unstable ones in the workspace. Moreover, on such singularities, the robot can freely move along a given direction without any constraint under the action of small perturbations.

We illustrate the singularity phenomena and their effects by simulations performed with two different continuum parallel robots.

***Index Terms*—Continuum parallel robots, Kinemato-statics, Singularity, Stability**

NOMENCLATURE OF THE MAIN SYMBOLS

$\boldsymbol{\lambda}$	Vector of Lagrange multipliers.
$\boldsymbol{\Phi}$	Vector of constraint equations.
$\mathbf{1}_p$	Identity matrix of dimension p.
$\mathbf{A}$, $\mathbf{P}$, $\mathbf{U}$	Robot kinematic Jacobian matrices related to the variables $\mathbf{q}_\mathrm{a}$, $\mathbf{q}_\mathrm{p}$ and $\mathbf{q}_\mathrm{u}$.
$\mathbf{c}_B$, $\mathbf{c}_r$	Passive joints constraints.
$\mathbf{c}_h$, c_h	Quaternions constraints.
$\mathbf{f}_i$, $\mathbf{m}_i$	Force and moment applied on the body i.
$\mathbf{g}$	Gravity field.
$\mathbf{H}$, $\mathbf{H}^r$	Full and reduced Hessian matrices.
$\mathbf{h}$	Vector of all robot legs quaternions.
$\mathbf{h}_i$	Quaternion associated with the frame $\mathcal{F}_i$.
L, ℓ	Lengths of a rod and of a finite element.
$\mathcal{L}$	A Lagrangian function.
$\mathbf{p}_i$, $\mathbf{p}_Q$	Positions of the origin of the frame $\mathcal{F}_i$, and of the point Q.
$\mathbf{q}_\mathrm{a}$, $\mathbf{q}_\mathrm{p}$, $\mathbf{q}_\mathrm{u}$	Motor, controlled and uncontrolled variables.
$\mathbf{q}_\mathrm{au}$, $\mathbf{q}_\mathrm{pu}$	Vectors $[\mathbf{q}_\mathrm{a}^T, \mathbf{q}_\mathrm{u}^T]^T$ and $[\mathbf{q}_\mathrm{p}^T, \mathbf{q}_\mathrm{u}^T]^T$.
$\mathbf{R}$, $\mathbf{T}$	Rotation and homogeneous transformation matrices.
V_e, V_g, V_w	Potential energies due to deformations, gravity or external wrenches.
$\mathbf{Z}$	A matrix spanning the null space of $\nabla_{\mathbf{q}_\mathrm{pu}} \boldsymbol{\Phi}^T$.

[1]S. Briot and A. Goldsztejn are with the Laboratoire des Sciences du Numérique at the CNRS, Nantes, France. {Sebastien.Briot, Alexandre.Goldsztejn}@ls2n.fr

I. INTRODUCTION

In order to improve the limited interaction capacities of rigid-link robot manipulators, researchers have proposed a new type of robot manipulators named continuum robots [1]. The concept for designing these robots was inspired by biological systems such as trunks, tentacles, chameleon tongues or also snakes [2]. Continuum robots are of interest for many applications related to manipulation in confined, or hard-to-reach workspace; especially, their use seems to be very promising for applications in minimally invasive surgery [3].

Most of continuum robots are designed with a serial architecture, in which rigid bodies and joints are replaced by a serial assembly of slender rods deformed by wires [4], [5], electromagnets [6], [7], fluidic actuators [8]–[10], shape memory alloy based actuators [11], [12], electro-active polymers [13], [14] or other types of actuation (e.g. concentric tube robots [15]–[17] or also multi-backbone robots [18]–[20]).

The concept of continuum parallel robots was first introduced in [21], [22]. These robots are made of several flexible elastic links arranged in parallel, connected at one extremity to a motor, and at the other extremity to a rigid moving platform. In [21], [22], continuum Gough-Stewart-like platforms were studied. Since these first works, several other architectures have been proposed: several continuum planar parallel robots have been detailed in [23]–[28] while a spatial three degrees-of-freedom (dof) has been studied in [29]. The concept of reconfigurable continuum parallel robots has also been investigated in [30].

The study of the continuum parallel robots started with the investigation of their geometrico-static modeling. In [21], [22], the robot legs were modeled using the Cosserat's rod theory, and the system of nonlinear ordinary differential equations characterizing the robot's equilibrium configurations was solved by a purely numerical approach. The works [23]–[26] are based on the the Kirchoff's rod theory, and the authors proposed a quasi-analytical description of the robot equilibrium configurations. This quasi-analytical form was obtained under the strict conditions that external wrenches apply on the platform only and deformations are planar. Moreover, in [23]–[26], wrenches applied on other bodies cannot be handled, and spatial robots cannot be modeled. However, the approach allows for finding all legs buckling modes.

Performances of these robots were investigated in several works. The papers [21], [26], [28], [29], [31] computed the workspace of several designs. Positioning error was studied in [28], [29]. In [28], the authors proposed a design able to reach nanometer accuracy, which is validated through

experimentations. Several indices of performance based on a numerical estimation of robot kinetostatic matrices were defined in [22] for studying the properties in terms of robot compliance, force transmission, and manipulability. The robot elastic stability was also investigated in several papers. The work [32] proposed a numerical test for evaluating stability, and defined a heuristic metric. More specifically, based on the analysis of the non-discretized ordinary differential equations (ODEs) characterizing the robot deformation, the authors showed that the robot static configuration is a minimizer of the potential energy, and that its stability can be assessed by analyzing the second-order conditions of calculus of variations. The authors of [26] identified several unstable configurations of continuum planar parallel robots. Additionally, they showed that some of the identified unstable configurations might correspond to singular configurations associated with the degeneracy of a local stiffness matrix. A few singular configurations of a compliance matrix (relating variations of wrenches applied to the robot platform with variations of the platform configuration) for a Gough-Stewart-like continuum parallel robots were also detected in [22], without any further analysis of the singularity problem.

Singularity analysis of robots is a crucial issue, because near singularities, robots lose some performance (for instance, ability to move along one given direction, or even stiffness and accuracy [33]). This is especially true for parallel robots, for which singularity analysis is more complex than for serial robots. Therefore, a lot of efforts have been dedicated to defining the singularities of rigid-link parallel robots [34]–[37], understanding the physical phenomena involved in them [38], [39], and finding the robot geometric configurations leading to them [40], [41] or their location in the workspace [42], [43]. Indeed, the parallel robot community has gained a deep understanding of singularities, their impact on the robot behavior, their analysis and their computation. The design of a parallel manipulator nowadays starts by the characterization and the computation of its parallel singularities.

On the opposite, singularities of continuum robots have been little investigated. Indeed, one of the main differences is that, contrary to their rigid-link counterparts, singular configurations cannot be found by studying the robot geometry: elasticity properties are also involved, meaning that the geometric tools developed for detecting singularities [40], [41] cannot apply anymore. Singularities of serial-like continuum robots have been studied for several designs (e.g. [9], [16], [44], [45]). As for rigid serial robots, the authors of these works showed that they correspond to a loss of mobility for the robot end-effector, and thus they define the workspace boundaries. However, to the best of our knowledge, the study of the singularities of continuum parallel robots is for the moment restricted to the detection of a few singular configurations for a limited number of robot architectures, like in [22], [26], [46]. Moreover, there remained a lack of a deep physical interpretation of the phenomena occurring in these detected singularities. We will show further that these physical phenomena are not limited to the problem of the loss of mobility. Indeed, this paper analyses the singularities of continuum parallel robots from the rigid parallel robot community point of view, allowing defining Type 1, Type 2 and Type 3 singularities [34] for continuum parallel robots in a coherent and meaningful way. As for rigid parallel robots, these singularities are shown to have a strong impact on workspace reachability, accuracy and stiffness performances.

In this paper, we define the singularity conditions for generic continuum parallel robots. This definition is based on the analysis of the expressions of the robot kinemato-static model[1], which results from differentiating the geometrico-static model. In order to compute the kinemato-static model, we first obtained the expressions of the total robot potential energy. Then, by computing the gradient and Hessian of the energy with respect to motor, end-effector and legs coordinates, the geometrico- and kinemato-static models can be obtained. We will show that the continuum parallel robots have several types of singularities: some of them correspond to workspace boundaries, some other to joint space boundaries, this latter being shown to be related to limits of stability in this paper.

By relating the expression of the Hessian matrix of the potential energy to the expression of some Jacobian matrices involved in the robot kinemato-static model, we were also able to provide an interpretation of the robot's behavior in singularities. Especially, we prove that some singularities appear when the Hessian matrix of the potential energy is rank deficient, i.e. when the robot potential energy has a local isovalue or, equivalently, when the robot reaches a limit of stability. Because of this property, we show that these singularities separate the workspace into different areas, some of them containing only stable configurations, the other containing only unstable ones. Moreover, on this singularity, the robot can freely move along a given direction without any constraint under the action of small perturbations.

It should be mentioned that, by reading both papers [22] and [32] in series, a link between singularities and limit of stability can be foreseen. Indeed, in [22], a singularity of a compliance matrix is observed (see Appendix B for the analysis of this singularity). In addition, in [32], it is shown that the instability is characterized by the degeneracy of a matrix relating the variation of the forces and the local motion of the deformable beam, which could be seen as a compliance matrix. However, those two matrices, even if somehow characterizing the same properties, are not equal, and therefore the link between singularities and limit of stability remains to be clearly established.

The paper is organized as follows. The next section deals with the computation of the potential energy of the continuum parallel robots. It is shown that the potential energy function depends on an augmented set of generalized coordinates which are not independent because of the closed-loop nature of the robot. In Section III, we derive the implicit geometrico-static model which is obtained thanks to the Lagrange conditions for minimizing a function under constraints. This implicit model must be solved numerically, and the stability conditions of its

[1]Following [47], we prefer to replace the word kinetostatic by the word kinemato-static: Indeed, the former is an assembly of the words kinetics and statics, and is not related with our present interest in kinematics, i.e. with the study of the motion.

solutions are detailed. This implicit geometrico-static model is used to derive the kinemato-static model in Section IV, from which conditions of singularity are deduced. Case studies are then analyzed in Section V. Finally, in Section VI, conclusions are drawn.

Notations

The Jacobian matrix $D\mathbf{f}(\mathbf{x}) \in \mathbb{R}^{m\times n}$ of a function $\mathbf{f} : \mathbb{R}^n \to \mathbb{R}^m$ is used to build linear approximations $\mathbf{f}(\mathbf{x}+\mathbf{h}) = \mathbf{f}(\mathbf{x}) + D\mathbf{f}(\mathbf{x})\mathbf{h} + o(\mathbf{h})$. The i^{th} line of the Jacobian matrix contains the derivatives with respect to each variable of the i^{th} component of the function: $D\mathbf{f}(\mathbf{x})_{i,j} = \frac{\partial f_i}{\partial x_j}$. The gradient of the $\mathbf{f}$ also contains partial derivatives but ordered differently: $\nabla\mathbf{f}(\mathbf{x}) = D\mathbf{f}(\mathbf{x})^T$. This convention usually used in the framework of optimization allows the gradient of a scalar valued function to be a vector, which is convenient in the context of optimization. Second order derivatives of a scalar valued function $f(\mathbf{x})$ are stacked together in the Hessian matrix $\nabla^2 f(\mathbf{x})$, whose entry (i,j) is $\frac{\partial^2 f(\mathbf{x})}{\partial x_i \partial x_j}$. Note that by Schwarz theorem, differentiation with respect to two variables commutes and the Hessian matrix is symmetric. The Hessian matrix can be defined by two consecutive derivations, but using gradient and derivative: $\nabla^2 f(\mathbf{x}) = D\nabla f(\mathbf{x})$. Using two derivatives consecutively instead leads to the third order tensor of second derivatives, which is less intuitive. In particular, non-square Hessian matrices can be defined by $\nabla^2_{\mathbf{x},\mathbf{y}} f(\mathbf{x},\mathbf{y}) = D_{\mathbf{x}}\nabla_{\mathbf{y}} f(\mathbf{x},\mathbf{y})$.

II. Potential Energy of the Continuum Parallel Robot

In this section, we provide the explicit expressions for the potential energy of the general class of continuum parallel robots described in Section II-A, which includes [22], [26]. We present the expressions of the potential energy of one single flexible rod in Section II-B, followed by the closed-loop mechanism potential energy involving several flexible rods and the platform in Section II-C. Finally, we discuss the mandatory discretization process of continuum parallel robots in Section II-D2 and provide a generic discretized parametrization of the robot configuration and potential energy in Section II-D1.

A. Description of the continuum parallel robot

Let us describe the generic continuum parallel robot architecture that we consider in this paper (Fig. 1): it is a robot which is made of n slender flexible rods (called legs). An extremity of each rod is connected to a motor at one end (points A_i, $i = 1,...,n$), the other extremity to the moving platform via a joint (at points B_i, $i = 1,...,n$), which is either a passive revolute joint, a passive spherical joint or a fixed joint, as proposed in [22], [26]. The legs can be either of constant length and connected at points A_i to an active revolute or prismatic joint as it was done in [26], or of variable length, i.e. acting like a soft cylinder fixed on the ground at point A_i as proposed in [22]. Other types of legs could be considered, by modifying the equations of the constraints

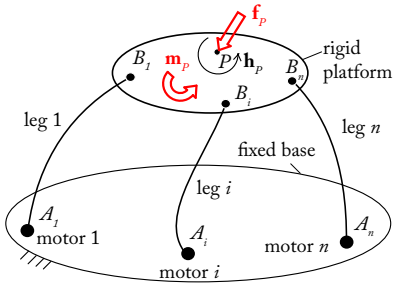

Fig. 1. A general continuum parallel robot

and the Jacobian matrices associated to the motions of the motors. The robot moving platform, on which is located the end-effector, is considered to be rigid.

The variable associated with the motor displacement for the leg i is denoted by q_{ai}. All motor variables are grouped in the vector $\mathbf{q}_{\text{a}}$. The variables associated with the platform motion are $\mathbf{p}_{\text{p}}$, the location of the platform center of mass P, and $\mathbf{h}_{\text{p}} = h_{\text{p1}} + h_{\text{p2}}\vec{\mathbf{i}} + h_{\text{p3}}\vec{\mathbf{j}} + h_{\text{p4}}\vec{\mathbf{k}}$ the unit quaternion (i.e. $\mathbf{h}_{\text{p}}^T\mathbf{h}_{\text{p}} = 1$) characterizing the platform orientation (Fig. 1).

Let us now compute the potential energy of the robot legs, which can be modeled as flexible rods of constant length clamped at points A_1 to A_n when the motors are fixed.

B. Potential energy of a single flexible rod

In this paper, we take the same hypotheses as in [26]: the rods are modeled using the Kirchoff assumptions (shear is neglected) and the rod elongation is considered to be negligible. More general assumptions, like the Cosserat ones [22], could be used without changing the definitions of the singularity conditions further.

We derive here the equations for the 3D problem. Equations for the 2D case can be found in [48]. Let us consider the leg i of the robot. It can be modeled as a slender rod of length L_i (Fig. 2) clamped into the ground at point A_i, made of an isotropic material and having a constant cross-section along its longitudinal direction. The robot base frame is denoted as $\mathcal{F}_0 : (O, \mathbf{d}_{01}, \mathbf{d}_{02}, \mathbf{d}_{03})$. The local configuration of a rod cross-section located at the curvilinear abscissa s is defined by the frame $\mathcal{F}_c : (S, \mathbf{d}_{i1}(s), \mathbf{d}_{i2}(s), \mathbf{d}_{i3}(s))$, in which $\mathbf{d}_{i3}(s)$ is the vector tangent to the cross-section at s. The configuration of the frame $\mathcal{F}_c$ with respect to (w.r.t.) the frame $\mathcal{F}_0$ is provided by the homogeneous transformation matrix ${}^0\mathbf{T}_s$ defined by:

$$ {}^0\mathbf{T}_s = \begin{bmatrix} {}^0\mathbf{R}_s & \mathbf{p}_i(s) \\ \mathbf{0} & 1 \end{bmatrix} \tag{1} $$

in which

$$ {}^0\mathbf{R}_s = \begin{bmatrix} {}^0\mathbf{d}_{i1}(s) & {}^0\mathbf{d}_{i2}(s) & {}^0\mathbf{d}_{i3}(s) \end{bmatrix} \tag{2} $$

is the rotation matrix between $\mathcal{F}_0$ and $\mathcal{F}_c$ and $\mathbf{p}_i(s)$ is the position of S in $\mathcal{F}_0$. Note that, in what follows, superscript "0" ("c", resp.) before any vector or matrix means that they are expressed in the frame $\mathcal{F}_0$ ($\mathcal{F}_c$, resp.).

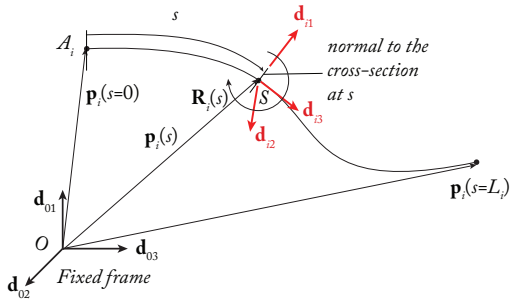

Fig. 2. Parameterization of the continuum clamped-free slender rod

The curvature and torsion of the rod can be represented by the Darboux vector $\mathbf{u}_i(s)$, defined as:

$$\mathbf{u}_i = \sum_{k=1}^{3} u_{ik}\,\mathbf{d}_{ik} \tag{3}$$

with [49]

$$u_{i1} = -\mathbf{d}_{i2}^T\,\mathbf{d}_{i3}',\ u_{i2} = -\mathbf{d}_{i3}^T\,\mathbf{d}_{i1}',\ u_{i3} = -\mathbf{d}_{i1}^T\,\mathbf{d}_{i2}' \tag{4}$$

in which $(.)'$ denotes the derivative w.r.t. the variable s, i.e. $(.)' = \partial(.)/\partial s$.

For an isotropic material, the rod deformation energy is then given by [50]:

$$V_{ei} = \frac{1}{2}\int_0^{L_i} ({}^c\mathbf{u}_i - {}^c\hat{\mathbf{u}}_i)^T \mathbf{K}_i ({}^c\mathbf{u}_i - {}^c\hat{\mathbf{u}}_i)\,ds \tag{5}$$

where $\hat{\mathbf{u}}_i = [\hat{u}_{i1}\ \hat{u}_{i2}\ \hat{u}_{i3}]^T$ is the (constant) pre-curvature of the rod, L_i is the rod length, and the matrix $\mathbf{K}_i$ is defined by:

$$\mathbf{K}_i = \mathrm{diag}([E_i\,I_{i1},\ E_i\,I_{i2},\ G_i\,I_{i0}]), \tag{6}$$

in which E_i is the material Young's modulus, G_i is its shear modulus, I_{i1} (I_{i2}, resp.) is the area moment of inertia of the cross-section around $\mathbf{d}_{i1}$ ($\mathbf{d}_{i2}$, resp.), and $I_{i0} = I_{i1} + I_{i2}$.

Let us now compute the potential energy due to the external wrenches. We assume that these wrenches are conservative and that only two types of external effects are applied on the rod:

- gravitational effects due to the gravity field $\mathbf{g}$ and
- any other external distributed forces.

The potential energy due to gravity is given by:

$$V_{gi} = -\mathbf{g}^T \rho_i \int_0^{L_i} \mathbf{p}_i(s)\,ds \tag{7}$$

with ρ_i the material linear density.

Let us finally denote as $\mathbf{f}_i$ a force distributed on the rod. The potential energy due to $\mathbf{f}_i$ is thus given by:

$$V_{wi} = -\int_0^{L_i} \mathbf{f}_i^T \mathbf{p}_i(s) ds \tag{8}$$

As a result, the total potential energy is equal to:

$$V_{\mathrm{rod}_i} = \sum_{j=1}^{N_i} (V_{eij} + V_{gij} + V_{wij}) \tag{9}$$

It should be noted that the total potential energy V_{rod_i} is provided in (9) under an integral form with the use of some functions which are unknowns (except at their boundaries due to the knowledge of the actuator position q_{ai}), in particular $\mathbf{u}_i(s)$. Note that $\mathbf{p}_i(s)$ can be obtained if $\mathbf{u}_i(s)$ is known.

C. Potential energy of the closed-loop mechanism

Considering now the full continuum parallel robot, its total potential energy is given by:

$$V_{\mathrm{tot}} = V_{\mathrm{platform}} + \sum_{i=1}^{n} V_{\mathrm{rod}_i} \tag{10}$$

where V_{platform} is the potential energy of the platform considered here as rigid. Its expression is given by

$$V_{\mathrm{platform}} = -\mathbf{f}_{\mathrm{p}}^T\,(\mathbf{p}_{\mathrm{p}} - \hat{\mathbf{p}}_{\mathrm{p}}) \tag{11}$$

$\mathbf{f}_{\mathrm{p}}$ is a constant force exerted on the robot platform at point P ($\mathbf{f}_{\mathrm{p}}$ includes the effect of the gravity field – recall that P is considered to the platform center of mass). A force $\mathbf{f}_{\mathrm{Q}}$ applied on the platform at any point Q with location $\mathbf{p}_{\mathrm{Q}}$ could be added as well, using the potential energy $-\mathbf{f}_{\mathrm{Q}}^T\,(\mathbf{p}_{\mathrm{Q}} - \hat{\mathbf{p}}_{\mathrm{Q}}) = \mathbf{f}_{\mathrm{Q}}^T\,(\mathbf{p}_{\mathrm{p}} + {}^0\mathbf{R}_{\mathrm{p}}\overrightarrow{PQ} - \hat{\mathbf{p}}_{\mathrm{Q}})$, but we disregard it in the rest of the computations. Moreover, 3D moment being non conservative [51], we do not consider them for the computation of the energy. However, they could easily be added later in Section III-A by using the Principle of Virtual Works. We have not included these additional technical details for the sake of clarity.

As a result, V_{tot} is a function of $\mathbf{p}_{\mathrm{p}}$ (and $\mathbf{h}_{\mathrm{p}}$ in a general case), of the leg deformation, and of course, of the motor locations $\mathbf{q}_{\mathrm{a}}$. It also depends on the loading, but the loading being considered constant, we do not add a variable in order to represent it.

Obviously, due to the closed kinematic chain geometric constraints (and of the quaternion constraints), variables $\mathbf{p}_{\mathrm{p}}$ and $\mathbf{h}_{\mathrm{p}}$ are related by the following expressions (for $i = 1, \ldots, n$):

$$c_{hp} = \mathbf{h}_{\mathrm{p}}^T\mathbf{h}_{\mathrm{p}} - 1 = 0 \tag{12}$$

$$\mathbf{c}_{Bi} = \mathbf{p}_{\mathrm{p}} + {}^0\mathbf{R}_{\mathrm{p}}\,\mathbf{r}_{PB_i} - \mathbf{p}_{B_i}(L_i) = \mathbf{0} \tag{13}$$

where $\mathbf{r}_{PB_i}$ is the vector $\overrightarrow{PB_i}$ expressed in the platform frame, and ${}^0\mathbf{R}_{\mathrm{p}}$ is the rotation matrix between the robot fixed frame $\mathcal{F}_0$ and the moving platform frame while $\mathbf{p}_{B_i}(L_i)$ is the location of point B_i obtained after computing the deformation of the leg i.

If the joint at B_i is spherical, Eqs. (12) and (13) are enough in order to characterize the platform constraints. If other joints are used (rigid or revolute joints), other constraints detailed [22] could be used.

In what follows, we stack all constraints in the vector $\mathbf{\Phi}$.

D. Discretized model

Subsection II-D1 describes the generic parametrization that is used in the paper, and the corresponding notations. Subsection II-D2 discusses classical approaches for discretization of the Cosserat rod potential energy.

1) Parametrization of the discretized model: The potential energy (10) depends on functional variables $\mathbf{u}_i(s)$ ($i = 1,\dots,n$). A practical way to analyse it is to discretize the functional variable $\mathbf{u}_i(s)$: they are each parametrized by a vector $\mathbf{h}_i \in \mathbb{R}^{N_i}$ of N_i real numbers. All these parameters are stacked into a vector $\mathbf{h} \in \mathbb{R}^{\sum N_i}$.

As expected, we will see below that the number of coordinates of the platform position and orientation that can be controlled is exactly the number $n = \dim \mathbf{q}_\mathrm{a}$ of actuated motors. Therefore, we define $\mathbf{q}_\mathrm{p} \in \mathbb{R}^n$ as the vector containing the coordinates to be controlled. Usually, it contains a subset of $(\mathbf{p}_\mathrm{p}, \mathbf{h}_\mathrm{p})$ of the platform position and orientation coordinates, but it may contain other types of variables, like in [52] where the authors controlled the five dof of the end-effector plus the robot collisions with six motors. Other types of variables (e.g. related to robot stiffness, leg curvature, etc) could also be defined. We stack all remaining coordinates amongst $(\mathbf{p}_\mathrm{p}, \mathbf{h}_\mathrm{p})$ and $\mathbf{h}$ to obtain the vector $\mathbf{q}_\mathrm{u} \in \mathbb{R}^m$ of uncontrolled coordinates. For notational convenience, we furthermore define $\mathbf{q}_\mathrm{pu} = (\mathbf{q}_\mathrm{p}, \mathbf{q}_\mathrm{u}) \in \mathbb{R}^{n+m}$ and $\mathbf{q} = (\mathbf{q}_\mathrm{a}, \mathbf{q}_\mathrm{p}, \mathbf{q}_\mathrm{u}) \in \mathbb{R}^{n+n+m}$. These coordinates are related by the system of equations $\mathbf{\Phi}(\mathbf{q}) = \mathbf{0}$, which contains geometric constraints as well as parametrization constraints like quaternion normalizations. The number of equations in $\mathbf{\Phi}(\mathbf{q}) = \mathbf{0}$ is denoted by $n_\Phi \leq n+m$. The integers n, m and n_Φ can be related to all variable numbers defined previously[2]. As already explained above, the total potential energy is denoted by V_tot and depends on all configuration variables $\mathbf{q}$.

2) Discussion on discretization processes: In [22], [53], the potential energy dependence on a non-discretized pose leads to a geometrico-static model of continuum parallel robots involving ODEs. The numerical strategy for solving the corresponding boundary value problems and evaluating the required robot Jacobian matrices relies on ODE solvers, which actually discretize the continuous model. In this work, we adopt a different strategy, based on a discretization of the potential energy equations. In addition of the conceptual and mathematical simplicity of having a finite number of pose coordinates in the potential energy expression, the numerical solving process does not include any ODE solver, which ease its implementation. This does not change the generality of the results in the definition and the physical interpretation of singularities. Singularities of continuum parallel robots are too complex to be formally investigated. The accuracy of the numerical investigations will depend on the discretization method and step-size, similarly to the ODE solver accuracy dependence on the ODE solver tolerance parameter.

There are several ways to discretize the potential energy, e.g., finite elements (e.g. [54], [55] for good surveys), assumed modes [56] or NURBS (Non-uniform rational basis splines, e.g. [57]). The simulations presented in Section V have been computed using finite differences[3], mainly aiming the simplicity of the derivation of the formal expression of the potential energies. Finite differences is a common way to solve the equations of continuum robots [50], [59]–[61], and more generally, to find the deformations of Cosserat rods [62]–[66]. They were also used in [48] for computing the geometrico-static model of a continuum planar parallel robot, and results showed that the accuracy of pose prediction is of less than 1 mm of error (for legs of 1 m discretized with 50 elements each) with respect to a pose computed by solving the system of constrained ODEs with a shooting method, like in [22].

III. Geometrico-static model

In the static context, configurations are acceptable provided that for fixed motor positions $\mathbf{q}_\mathrm{a}$ they are stable equilibrium with respect to internal and external forces. This leads to the definitions of the geometrico-static model, which relates fixed motor positions and stable configurations, as well as of the related forward and inverse problems. In Section III-A, we derive the equations of the geometrico-static model. The stability of its solutions is discussed Section III-B. For the sake of clarity, external wrenches do not appear explicitly in this generic model that we propose. They play formally the same role as active joints coordinates, i.e., they are fixed to constant values for the derivation of the geometrico-static model.

A. The geometrico-static model and its forward and inverse problems

a) The geometrico-static model: As mentioned previously, acceptable robot configurations are static equilibria for fixed $\mathbf{q}_\mathrm{a}$. This requirement is satisfied if and only if $\mathbf{q}_\mathrm{pu}$ is a local minimizer of the potential energy $V_\mathrm{tot}(\mathbf{q})$ associated to the system. Since coordinates $\mathbf{q}$ are related by the system of equations $\mathbf{\Phi}(\mathbf{q}) = \mathbf{0}$, the local extrema (e.g., minimizer, maximizer or saddle point) of the potential energy are characterized by the Lagrange conditions [67]. Local minimizers have to satisfy additional conditions related to second order derivatives, which are detailed in Section III-B.

Lagrange conditions provide the following characterization of local extrema: Under the condition that the gradients of the equality constraint are linearly independent, i.e., $\nabla_{\mathbf{q}_\mathrm{pu}} \mathbf{\Phi}(\mathbf{q})$ is full rank, $\mathbf{q}$ is a local extrema if and only if there exist multipliers $\boldsymbol{\lambda} \in \mathbb{R}^{n_\Phi}$ such that

$$\nabla_{\mathbf{q}_\mathrm{pu}} V_\mathrm{tot}(\mathbf{q}) + \nabla_{\mathbf{q}_\mathrm{pu}} \mathbf{\Phi}(\mathbf{q})\, \boldsymbol{\lambda} = \mathbf{0} \tag{14}$$

$$\mathbf{\Phi}(\mathbf{q}) = \mathbf{0}. \tag{15}$$

This system of equations represents the implicit geometrico-static model. The explicit expressions of these equations can be obtained in an analytical way[4]. Note that the expression in

[2]For instance in the spatial case with $n = 6$ actuated legs modeled with $N_i = N$ elements and passive spherical joints connecting the legs to the platform, we have $\mathbf{q}_\mathrm{a} \in \mathbb{R}^6$, $(\mathbf{p}_\mathrm{p}, \mathbf{h}_\mathrm{p}) \in \mathbb{R}^7$ but $\mathbf{q}_\mathrm{p} \in \mathbb{R}^6$ (usually $\mathbf{q}_\mathrm{p}$ contains $\mathbf{p}_\mathrm{p}$ and three coordinates of $\mathbf{h}_\mathrm{p}$) and therefore $\mathbf{h} \in \mathbb{R}^{4(N-1)n}$ and $\mathbf{q}_\mathrm{u} \in \mathbb{R}^m$ with $m = 4(N-1)n + 1$ (since $\mathbf{q}_\mathrm{u}$ contains $\mathbf{h}$ and the coordinate of $\mathbf{h}_\mathrm{p}$ that is not included in $\mathbf{q}_\mathrm{p}$). Finally, if $\mathbf{h}$ contains quaternions, $n_\Phi = (N-1)n + 1 + 3n$ since we have $N-1$ quaternion constraints for each leg plus one quaternion constraint for the platform, and 3 constraints per leg for the spherical joints.

[3]All details for obtaining the expression of the potential energy V_tot in (10) and all of its first and second derivatives, i.e. all expressions of the geometrico-static and kinemato-static models defined thereafter, computed with finite differences are provided in the technical report [58].

[4]Although the implicit geometrico-static model has a closed form expression, its solutions do not have any closed form. Therefore, some local numerical descent-like method will have to be used to solve it in Section V.

the left-hand side of Equation (14) is the gradient $\nabla_{\mathbf{q}_{\rm pu}}\mathcal{L}(\mathbf{q},\boldsymbol{\lambda})$ of the so-called Lagrangian function

$$\mathcal{L}(\mathbf{q},\boldsymbol{\lambda}) = V_{\rm tot}(\mathbf{q}) + \boldsymbol{\Phi}(\mathbf{q})^T\boldsymbol{\lambda} \tag{16}$$

associated to the equality constrained optimization problem. As usually when using Lagrange conditions for solving an equality-constrained optimization problem, the configurations $\mathbf{q}$ that make $\nabla_{\mathbf{q}_{\rm pu}}\boldsymbol{\Phi}(\mathbf{q})$ not full rank have to be investigated since they may turn out to be local minimizers that do not satisfy the Lagrange conditions (14)–(15), but in our context they lead to uninteresting configurations that might appear only when several legs are fully extended (see Section IV-B4).

b) The forward and inverse geometrico-static problems: The implicit geometrico-static model (14)–(15) is a system of $n+m+n_\Phi$ equations and $2n+m+n_\Phi$ unknowns. As a consequence, fixing n variables to desired values gives rise to a square system of equations, having generically a finite number of solutions. The *forward geometrico-static problem* consists in fixing the n motor positions $\mathbf{q}_{\rm a}$ to some desired values and to compute the corresponding n controlled coordinates, the uncontrolled coordinates $\mathbf{q}_{\rm pu}$ and the Lagrange multipliers $\boldsymbol{\lambda}$ so that $(\mathbf{q},\boldsymbol{\lambda}) = (\mathbf{q}_{\rm a},\mathbf{q}_{\rm p},\mathbf{q}_{\rm u},\boldsymbol{\lambda})$ is solution to the implicit geometrico-static model (14)–(15). The *inverse geometrico-static problem* consists in fixing the n controlled coordinates $\mathbf{q}_{\rm p}$ to some desired values and to compute the corresponding n motor positions $\mathbf{q}_{\rm a}$, the uncontrolled coordinates $\mathbf{q}_{\rm u}$ and the Lagrange multipliers $\boldsymbol{\lambda}$ so that $(\mathbf{q},\boldsymbol{\lambda})$ is solution to the implicit geometrico-static model (14)–(15).

In both cases, the computed configurations $\mathbf{q}_{\rm a}$, $\mathbf{q}_{\rm p}$ and $\mathbf{q}_{\rm u}$ are only local extrema that must be additionally checked to be local minimizers of the potential energy, i.e., to be actual stable configurations. The computed multipliers $\boldsymbol{\lambda}$ are not useful in practice, but they actually have to be computed when solving Lagrange conditions associated to an equality constrained optimization problem and they are necessary to assess the stability of the associated solution. The conditions for the stability of the computed local extrema are detailed in the next section.

B. Stability of the solutions

The local extrema $\mathbf{q} = (\mathbf{q}_{\rm a},\mathbf{q}_{\rm p},\mathbf{q}_{\rm u})$ computed using the implicit geometrico-static model (14)–(15) are stable if and only if they correspond to local minimizers of the potential energy subject to the constraints $\boldsymbol{\Phi}(\mathbf{q}) = \mathbf{0}$. The second order Lagrange conditions provide sufficient conditions for this, which are now recalled. See, e.g., [67] for a detailed description.

We consider a local extrema $\mathbf{q}^*_{\rm pu}$ associated to fixed motor positions $\mathbf{q}^*_{\rm a}$. As previously, we suppose from now on that $\nabla_{\mathbf{q}_{\rm pu}}\boldsymbol{\Phi}(\mathbf{q}^*)$ is of full rank. Checking whether a local extrema $\mathbf{q}^*$ is a local minimizer or not requires determining the second order behavior of the potential energy versus the constraints curvature inside the tangent space of the constraints. To this end, one must have computed the Lagrange multipliers $\boldsymbol{\lambda}^*$ corresponding to $\mathbf{q}^*$, and furthermore we must have computed both:

- The Hessian matrix $\mathbf{H} = \nabla^2_{\mathbf{q}_{\rm pu},\mathbf{q}_{\rm pu}}\mathcal{L}(\mathbf{q}^*_{\rm pu},\boldsymbol{\lambda}^*)$ of the Lagrangian function. It has $n+m$ lines and columns and expresses the second order interaction of the potential energy and the constraints in a neighborhood of $\mathbf{q}^*_{\rm pu}$.
- A matrix $\mathbf{Z}$ whose columns span the null space of $\nabla_{\mathbf{q}_{\rm pu}}\boldsymbol{\Phi}(\mathbf{q}^*)^T$. This matrix has $n+m-n_\Phi$ orthonormal columns of size $n+m$, and satisfies $\nabla_{\mathbf{q}_{\rm pu}}\boldsymbol{\Phi}(\mathbf{q}^*)^T\mathbf{Z} = \mathbf{0}$.

Under the previously stated condition that $\nabla_{\mathbf{q}_{\rm pu}}\boldsymbol{\Phi}(\mathbf{q}^*)$ is full rank, the columns of $\mathbf{Z}$ also span the tangent space of the manifold defined by the constraints $\boldsymbol{\Phi}(\mathbf{q}_{\rm a},\mathbf{q}_{\rm pu}) = \mathbf{0}$ in the space of $\mathbf{q}_{\rm pu}$, for $\mathbf{q}_{\rm a}$ fixed to $\mathbf{q}^*_{\rm a}$. As a consequence, the restriction to this tangent space of the second order information encoded in the Hessian matrix $\mathbf{H}$ is obtained by a change of basis using the columns of $\mathbf{Z}$, leading to the formulation of the reduced Hessian matrix

$$\mathbf{H}^r = \mathbf{Z}^T\mathbf{H}\mathbf{Z}. \tag{17}$$

Formally, feasible variations $\Delta\mathbf{q}_{\rm pu}$ in a neighborhood of $\mathbf{q}_{\rm pu}$, i.e., variations in the tangent space of the constraints, have the form $\Delta\mathbf{q}_{\rm pu} = \mathbf{Z}\Delta\mathbf{v}$ for some $\Delta\mathbf{v}$. Then we have

$$V_{\rm tot}(\mathbf{q}_{\rm a},\mathbf{q}_{\rm pu}+\mathbf{Z}\Delta\mathbf{v}) \approx V_{\rm tot}(\mathbf{q}_{\rm a},\mathbf{q}_{\rm pu}) + \frac{1}{2}\Delta\mathbf{v}^T\,\mathbf{H}^r\Delta\mathbf{v}. \tag{18}$$

Since (18) provides a quadratic approximation of the energy in the tangent space of the constraints, the matrix $\mathbf{H}^r$ can be interpreted as the Hessian of the energy with respect to a set of generalized coordinates. Although this is a classical result in optimization, Appendix A provides the mathematical details to obtain (18) in a way that it enlightens this relationship. As a consequence, the stability properties of the potential energy $V_{\rm tot}(\mathbf{q})$ subject to the constraint $\boldsymbol{\Phi}(\mathbf{q}) = \mathbf{0}$ are deduced from the unconstrained stability conditions applied to the reduced Hessian $\mathbf{H}^r$:

- If all eigenvalues of $\mathbf{H}^r$ are positive, $\mathbf{q}^*_{\rm pu}$ is a minimum of the potential energy leading to a stable solution (Fig. 3(a)).
- If all eigenvalues of $\mathbf{H}^r$ are negative, $\mathbf{q}^*_{\rm pu}$ is a maximum of the potential energy leading to an unstable solution (Fig. 3(b)).
- If some eigenvalues of $\mathbf{H}^r$ positive and some other negative, $\mathbf{q}^*_{\rm pu}$ is a saddle point of the potential energy also leading to an unstable solution (Fig. 3(c)).
- If at least one eigenvalue of $\mathbf{H}^r$ is zero, the stability of $\mathbf{q}^*_{\rm pu}$ cannot be assessed by the second order model, and there is an isovalue of the potential energy along the directions represented by the eigenvectors associated with the null eigenvalues (Fig. 3(d)).

This latter case is associated to a singularity condition, as explained in the next section, which is dedicated to the singularity analysis.

IV. Kinemato-static Modeling and Singularity Conditions

In this Section, we give the expression of the kinemato-static model and we provide the conditions of singularity. Again for the sake of clarity, the kinemato-static model is derived here without considering external wrenches, which are considered to be constant. Furthermore, external wrenches are not involved in the definition of singularities. The straightforward extension of the kinemato-static model to include external wrenches and their variations are presented in Appendix B.

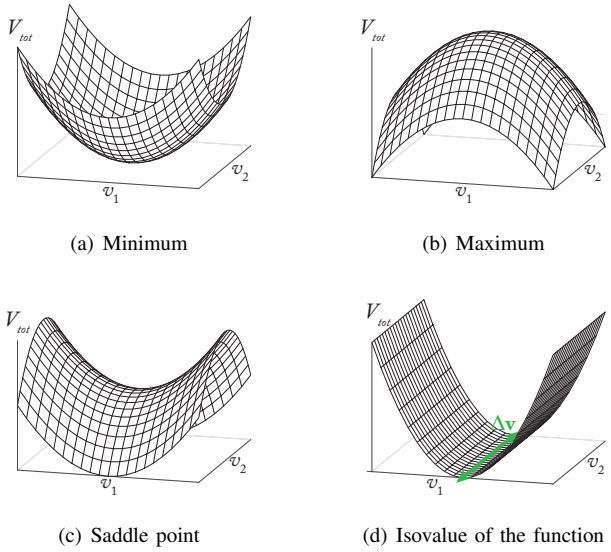

(a) Minimum (b) Maximum

(c) Saddle point (d) Isovalue of the function

Fig. 3. Stability of the solution for a potential energy function V_{tot} of two generalized coordinates x_1 and x_2

A. Derivation of the kinemato-static equations

The kinemato-static model of the robot can be obtained by differentiating the equations (14) and (15) w.r.t. all variables $\mathbf{q}_{\mathrm{a}} \in \mathbb{R}^n$, $\mathbf{q}_{\mathrm{p}} \in \mathbb{R}^n$ and $\mathbf{q}_{\mathrm{u}} \in \mathbb{R}^m$, and with respect to multipliers $\boldsymbol{\lambda} \in \mathbb{R}^{n_\Phi}$ as well. We obtain the following linear relations relating the variations $\Delta\mathbf{q}_{\mathrm{a}}$, $\Delta\mathbf{q}_{\mathrm{p}}$, $\Delta\mathbf{q}_{\mathrm{u}}$ and $\Delta\boldsymbol{\lambda}$ of variables and multipliers:

$$\mathbf{A}_{\mathcal{L}}\,\Delta\mathbf{q}_{\mathrm{a}} + \mathbf{P}_{\mathcal{L}}\,\Delta\mathbf{q}_{\mathrm{p}} + \mathbf{U}_{\mathcal{L}}\,\Delta\mathbf{q}_{\mathrm{u}} + \boldsymbol{\Lambda}_{\mathcal{L}}\,\Delta\boldsymbol{\lambda} = \mathbf{0} \quad (19)$$

$$\mathbf{A}_{\Phi}\,\Delta\mathbf{q}_{\mathrm{a}} + \mathbf{P}_{\Phi}\,\Delta\mathbf{q}_{\mathrm{p}} + \mathbf{U}_{\Phi}\,\Delta\mathbf{q}_{\mathrm{u}} = \mathbf{0} \quad (20)$$

where

- $\mathbf{A}_{\mathcal{L}} = D_{\mathbf{q}_{\mathrm{a}}} \nabla_{\mathbf{q}_{\mathrm{pu}}} \mathcal{L}(\mathbf{q}, \boldsymbol{\lambda}) \in \mathbb{R}^{(n+m)\times n}$,
- $\mathbf{P}_{\mathcal{L}} = D_{\mathbf{q}_{\mathrm{p}}} \nabla_{\mathbf{q}_{\mathrm{pu}}} \mathcal{L}(\mathbf{q}, \boldsymbol{\lambda}) \in \mathbb{R}^{(n+m)\times n}$,
- $\mathbf{U}_{\mathcal{L}} = D_{\mathbf{q}_{\mathrm{u}}} \nabla_{\mathbf{q}_{\mathrm{pu}}} \mathcal{L}(\mathbf{q}, \boldsymbol{\lambda}) \in \mathbb{R}^{(n+m)\times m}$,
- $\boldsymbol{\Lambda}_{\mathcal{L}} = D_{\boldsymbol{\lambda}} \nabla_{\mathbf{q}_{\mathrm{pu}}} \mathcal{L}(\mathbf{q}, \boldsymbol{\lambda}) = \nabla_{\mathbf{q}_{\mathrm{pu}}} \boldsymbol{\Phi}(\mathbf{q}) \in \mathbb{R}^{(n+m)\times n_\Phi}$,
- $\mathbf{A}_{\Phi} = D_{\mathbf{q}_{\mathrm{a}}} \boldsymbol{\Phi}(\mathbf{q}) \in \mathbb{R}^{n_\Phi \times n}$,
- $\mathbf{P}_{\Phi} = D_{\mathbf{q}_{\mathrm{p}}} \boldsymbol{\Phi}(\mathbf{q}) \in \mathbb{R}^{n_\Phi \times n}$, and
- $\mathbf{U}_{\Phi} = D_{\mathbf{q}_{\mathrm{u}}} \boldsymbol{\Phi}(\mathbf{q}) \in \mathbb{R}^{n_\Phi \times m}$.

Note that grouping together $\mathbf{P}_{\mathcal{L}}$ and $\mathbf{U}_{\mathcal{L}}$ leads to the standard Hessian matrix of the Lagrangian function:

$$\begin{bmatrix}\mathbf{P}_{\mathcal{L}} & \mathbf{U}_{\mathcal{L}}\end{bmatrix} = D_{\mathbf{q}_{\mathrm{pu}}} \nabla_{\mathbf{q}_{\mathrm{pu}}} \mathcal{L}(\mathbf{q}, \boldsymbol{\lambda}) = \nabla^2_{\mathbf{q}_{\mathrm{pu}}, \mathbf{q}_{\mathrm{pu}}} \mathcal{L}(\mathbf{q}, \boldsymbol{\lambda}) = \mathbf{H}. \quad (21)$$

This relationship between the matrices $\mathbf{P}_{\mathcal{L}}$ and $\mathbf{U}_{\mathcal{L}}$ involved in the kinemato-static model and the Hessian of the Lagrangian of total potential energy gives rise to a characterization of Type 2 singularities in terms of potential energy. This is detailed in Section IV-B (see Equation (30)).

The system of equation (19), (20) is composed of $n+m+n_\Phi$ equations and $2n + m + n_\Phi$ unknowns, which are $\Delta\mathbf{q}_{\mathrm{a}}$, $\Delta\mathbf{q}_{\mathrm{p}}$, $\Delta\mathbf{q}_{\mathrm{u}}$, $\Delta\boldsymbol{\lambda}$. For the kinemato-static analysis, there is little interest to characterize the variations $\Delta\boldsymbol{\lambda}$ w.r.t. to the others. Furthermore, as explained further in Section IV-B4, the degeneracy of the matrix $\boldsymbol{\Lambda}_{\mathcal{L}} = \nabla_{\mathbf{q}_{\mathrm{pu}}} \Phi(\mathbf{q})$ is unlikely and uninteresting in practice. Therefore, it is worthy to eliminate the multipliers variations $\Delta\boldsymbol{\lambda}$ from the system of equations, reaching this way a kinemato-static model with $n + m$ equations and $2n + m$ unknowns closer to the physical intuition. Eliminating $\Delta\boldsymbol{\lambda}$ using Gaussian elimination does not lead to any usable explicit formula. Therefore, we use instead the nullspace $\mathbf{Z}$ of the matrix $\boldsymbol{\Lambda}_{\mathcal{L}}^T = \nabla_{\mathbf{q}_{\mathrm{pu}}} \boldsymbol{\Phi}(\mathbf{q})^T$, which satisfies $\mathbf{Z}^T \boldsymbol{\Lambda}_{\mathcal{L}} = \mathbf{0}$ by definition of the nullspace. Under the assumption that $\boldsymbol{\Lambda}_{\mathcal{L}}$ is full rank, the matrix $[\mathbf{Z}\,\boldsymbol{\Lambda}_{\mathcal{L}}]$ is square of size $n + m$ and nonsingular. Therefore, left-multiplying (19) by the nonsingular square matrix $[\mathbf{Z}\,\boldsymbol{\Lambda}_{\mathcal{L}}]^T$ gives rise to an equivalent system:

$$\begin{aligned}[\mathbf{A}_{\mathcal{L}}\,\mathbf{P}_{\mathcal{L}}\,\mathbf{U}_{\mathcal{L}}\,\boldsymbol{\Lambda}_{\mathcal{L}}] \begin{bmatrix}\Delta\mathbf{q}\\ \Delta\boldsymbol{\lambda}\end{bmatrix} = \mathbf{0} \iff \\ \begin{bmatrix}\mathbf{Z}^T\\ \boldsymbol{\Lambda}_{\mathcal{L}}^T\end{bmatrix} [\mathbf{A}_{\mathcal{L}}\,\mathbf{P}_{\mathcal{L}}\,\mathbf{U}_{\mathcal{L}}\,\boldsymbol{\Lambda}_{\mathcal{L}}] \begin{bmatrix}\Delta\mathbf{q}\\ \Delta\boldsymbol{\lambda}\end{bmatrix} = \mathbf{0}\end{aligned} \quad (22)$$

By expanding this block-matrix product and using $\mathbf{Z}^T\boldsymbol{\Lambda}_{\mathcal{L}} = \mathbf{0}$, we obtain the following block-triangularized system equivalent to (19):

$$\mathbf{Z}^T\,[\mathbf{A}_{\mathcal{L}}\,\mathbf{P}_{\mathcal{L}}\,\mathbf{U}_{\mathcal{L}}]\,\Delta\mathbf{q} = \mathbf{0} \quad (23)$$

$$\boldsymbol{\Lambda}_{\mathcal{L}}^T\,[\mathbf{A}_{\mathcal{L}}\,\mathbf{P}_{\mathcal{L}}\,\mathbf{U}_{\mathcal{L}}]\,\Delta\mathbf{q} + \boldsymbol{\Lambda}_{\mathcal{L}}^T\,\boldsymbol{\Lambda}_{\mathcal{L}}\,\Delta\boldsymbol{\lambda} = \mathbf{0}. \quad (24)$$

As explained in the previous section, the matrix $\mathbf{Z}$ has $n + m - n_\Phi$ columns. Therefore $\mathbf{Z}^T\mathbf{A}_{\mathcal{L}}$, $\mathbf{Z}^T\mathbf{P}_{\mathcal{L}}$ and $\mathbf{Z}^T\mathbf{U}_{\mathcal{L}}$ all have $n + m - n_\Phi$ rows. On the other hand, $\mathbf{A}_{\Phi}$, $\mathbf{P}_{\Phi}$ and $\mathbf{U}_{\Phi}$ all have n_Φ rows. Therefore, we can group Equation (23) and Equation (20) to obtain the final expression of the kinemato-static model

$$\mathbf{A}\,\Delta\mathbf{q}_{\mathrm{a}} + \mathbf{P}\,\Delta\mathbf{q}_{\mathrm{p}} + \mathbf{U}\,\Delta\mathbf{q}_{\mathrm{u}} = \mathbf{0}, \quad (25)$$

where $\mathbf{A} \in \mathbb{R}^{(n+m)\times n}$, $\mathbf{P} \in \mathbb{R}^{(n+m)\times n}$, $\mathbf{U} \in \mathbb{R}^{(n+m)\times m}$, and

$$\mathbf{A} = \begin{bmatrix}\mathbf{Z}^T\mathbf{A}_{\mathcal{L}}\\ \mathbf{A}_{\Phi}\end{bmatrix},\ \mathbf{P} = \begin{bmatrix}\mathbf{Z}^T\mathbf{P}_{\mathcal{L}}\\ \mathbf{P}_{\Phi}\end{bmatrix} \text{ and } \mathbf{U} = \begin{bmatrix}\mathbf{Z}^T\mathbf{U}_{\mathcal{L}}\\ \mathbf{U}_{\Phi}\end{bmatrix}. \quad (26)$$

Once a solution $\Delta\mathbf{q}$ of (25) has been computed, the corresponding multiplier variations can be obtained by left-multiplying (24) by $(\boldsymbol{\Lambda}_{\mathcal{L}}^T\,\boldsymbol{\Lambda}_{\mathcal{L}})^{-1}$, leading to

$$\Delta\boldsymbol{\lambda} = -\boldsymbol{\Lambda}_{\mathcal{L}}^{+}\,[\mathbf{A}_{\mathcal{L}}\,\mathbf{P}_{\mathcal{L}}\,\mathbf{U}_{\mathcal{L}}]\,\Delta\mathbf{q}. \quad (27)$$

Note that the same elimination process could be used to eliminate the variables $\Delta\mathbf{q}_{\mathrm{u}}$ from (25) provided that $\mathbf{U}$ is full rank. This would lead to a direct linear relationship between $\Delta\mathbf{q}_{\mathrm{a}}$ and $\Delta\mathbf{q}_{\mathrm{p}}$, as in [22], [53]. However, the variables $\mathbf{q}_{\mathrm{u}}$ and their variations $\Delta\mathbf{q}_{\mathrm{u}}$ are meaningful and eliminating them may hide some singularities (namely leg singularities defined in Section IV-B).

The kinemato-static model (25) has $2n + m$ unknowns and $n + m$ linear equations. Therefore, a square system of equations is obtained by fixing either $\Delta\mathbf{q}_{\mathrm{a}}$ or $\Delta\mathbf{q}_{\mathrm{p}}$, leading to the forward and inverse kinemato-static problems:

- *Forward kinemato-static problem*: Given $\Delta\mathbf{q}_{\mathrm{a}} \in \mathbb{R}^n$, compute $\Delta\mathbf{q}_{\mathrm{p}}$ and $\Delta\mathbf{q}_{\mathrm{u}}$ by solving the linear system (25), which becomes a system of $n + m$ equations and $n + m$ unknowns. Provided that matrix $\begin{bmatrix}\mathbf{P}\ \mathbf{U}\end{bmatrix}$ is nonsingular, the solution of the forward kinemato-static problem is

$$\begin{bmatrix}\Delta\mathbf{q}_{\mathrm{p}}\\ \Delta\mathbf{q}_{\mathrm{u}}\end{bmatrix} = -\begin{bmatrix}\mathbf{P}\ \mathbf{U}\end{bmatrix}^{-1}\mathbf{A}\ \Delta\mathbf{q}_{\mathrm{a}}. \quad (28)$$

- *Inverse kinemato-static problem*: Given $\Delta\mathbf{q}_\mathrm{p} \in \mathbb{R}^n$, compute $\Delta\mathbf{q}_\mathrm{a}$ and $\Delta\mathbf{q}_\mathrm{u}$ by solving the linear system (25), which becomes again a system of $n+m$ equations and $n+m$ unknowns. Provided that matrix $\begin{bmatrix}\mathbf{A} & \mathbf{U}\end{bmatrix}$ is nonsingular, the solution of the inverse kinemato-static problem is

$$\begin{bmatrix}\Delta\mathbf{q}_\mathrm{a} \\ \Delta\mathbf{q}_\mathrm{u}\end{bmatrix} = -\begin{bmatrix}\mathbf{A} & \mathbf{U}\end{bmatrix}^{-1}\mathbf{P}\ \Delta\mathbf{q}_\mathrm{p}. \tag{29}$$

The non-solvability of the forward and inverse kinemato-static problems due to the nonregularity of the matrices to be inverted in (28) and (29) leads to the main conditions of singularities, which are analyzed in the next Section.

B. Singularity conditions

1) Singularities of the matrix $[\mathbf{A}\ \ \mathbf{U}]$*, for matrices* $\mathbf{A}$ *and* $\mathbf{U}$ *full rank:* When this matrix is singular, there exist small non null motions $\Delta\mathbf{q}_\mathrm{a}$ and $\Delta\mathbf{q}_\mathrm{u}$ that belong to the kernel of the matrix $[\mathbf{A}\ \ \mathbf{U}]$, for which $\Delta\mathbf{q}_\mathrm{p}$ is equal to $\mathbf{0}$. This means that, for such configurations, the end-effector cannot move along some desired controlled directions. Additionally, in the neighborhood of these areas, a large displacement of the motors will lead to a small displacement of the end-effector.

In [34] for rigid parallel robots, singularities of the inverse geometric model are called as Type 1 singularities. Similarly, in the rest of the paper, we denote as Type 1 singularities the singularities studied in this subsection.

2) Singularities of the matrix $[\mathbf{P}\ \ \mathbf{U}]$*, for matrices* $\mathbf{P}$ *and* $\mathbf{U}$ *full rank:* When this matrix is singular, there exist small non null motions $\Delta\mathbf{q}_\mathrm{p}$ and $\Delta\mathbf{q}_\mathrm{u}$ that belong to the kernel of the matrix $[\mathbf{P}\ \ \mathbf{U}]$, for which $\Delta\mathbf{q}_\mathrm{a}$ is equal to $\mathbf{0}$. This means that, in such configurations, for certain motions of the legs and of the platform, there is no motion of the motors. Additionally, in the neighborhood of these areas, a small displacement of the motors will lead to a large displacement of the end-effector.

In [34] for rigid parallel robots, singularities of the forward geometric model are called as Type 2 singularities. In the same vein, in the rest of the paper, we denote as Type 2 singularities the singularities studied in this subsection. These singularities correspond to the boundaries of the robot active joint space[5], and for which the end-effector cannot anymore resist to wrenches applied along given directions (Fig. 4(b)).

As explained earlier, Eq. (21) relates Type 2 singularities to the potential energy. Formally, from Eqs. (21) and (26), we obtain

$$[\mathbf{P}\ \ \mathbf{U}] = \begin{bmatrix}\mathbf{Z}^T\mathbf{H} \\ \nabla_{\mathbf{q}_\mathrm{p}}\mathbf{\Phi}(\mathbf{q})^T\ \nabla_{\mathbf{q}_\mathrm{u}}\mathbf{\Phi}(\mathbf{q})^T\end{bmatrix} = \begin{bmatrix}\mathbf{Z}^T\mathbf{H} \\ \nabla_{\mathbf{q}_\mathrm{pu}}\mathbf{\Phi}(\mathbf{q})^T\end{bmatrix}. \tag{30}$$

As a consequence, in Type 2 singularities $[\mathbf{P}\ \ \mathbf{U}]$ is singular, and this happens if and only if there exists a vector $\mathbf{u} \neq \mathbf{0}$ such that both $\mathbf{Z}^T\mathbf{H}\mathbf{u} = \mathbf{0}$ and $\nabla_{\mathbf{q}_\mathrm{pu}}\mathbf{\Phi}(\mathbf{q})^T\mathbf{u} = \mathbf{0}$. The matrix $\mathbf{Z}$ being the kernel of $\nabla_{\mathbf{q}_\mathrm{pu}}\mathbf{\Phi}(\mathbf{q})^T$ we have $\mathbf{u} = \mathbf{Z}\mathbf{v}$ for some $\mathbf{v} \neq \mathbf{0}$. Finally, $[\mathbf{P}\ \ \mathbf{U}]$ is singular if and only there exists $\mathbf{v} \neq \mathbf{0}$ such that $\mathbf{Z}^T\mathbf{H}\mathbf{Z}\mathbf{v} = \mathbf{H}^r\mathbf{v} = \mathbf{0}$. This means that the matrix $[\mathbf{P}\ \ \mathbf{U}]$ is singular if and only if the matrix $\mathbf{H}^r$ is singular. From the Section III-B, we conclude that these singularities correspond to isovalues of the potential energy during motions along the direction $\mathbf{v}$. This also means that the robot can move along the direction $\mathbf{v}$ without any constraints under the action of small perturbation, i.e. the robot has zero local stiffness along the direction $\mathbf{v}$. Another consequence is that the set of stable solutions, which have only positive eigenvalues for $\mathbf{H}^r$, and the set of unstable solutions, which have at least one negative eigenvalue for $\mathbf{H}^r$, are necessarily separated by a set of configurations that have a null eigenvalue for $\mathbf{H}^r$. In other words, the sets of stable and unstable configurations are separated by Type 2 singularity loci. Note that however it may also happen that Type 2 singularities separate sets of stable configurations as well, or sets of unstable configurations. The former case is non-typical since a zero eigenvalue would be surrounded by positive eigenvalues only. The later case is generic when the number of negative eigenvalues increases, but of low interest since all these configurations are unstable.

3) $[\mathbf{A}\ \ \mathbf{U}]$ *and* $[\mathbf{P}\ \ \mathbf{U}]$ *are both singular, for matrices* $\mathbf{A}$*,* $\mathbf{P}$*, and* $\mathbf{U}$ *full rank:* This type of singularity is similar to the Type 3 singularities described in [34]. In the same time, we lose the ability to move along one given direction

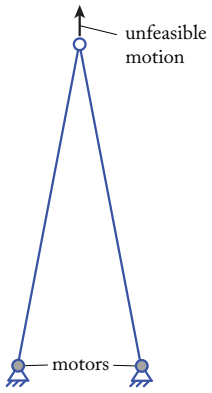

(a) Example of singularity for $[\mathbf{A}\ \mathbf{U}]$, for matrices $\mathbf{A}$ and $\mathbf{U}$ full rank: the robot reached the boundaries of the workspace

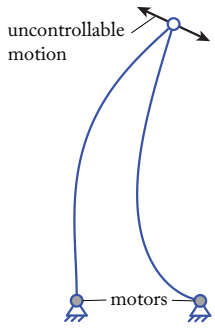

(b) Example of singularity for $[\mathbf{P}\ \mathbf{U}]$, for matrices $\mathbf{P}$ and $\mathbf{U}$ full rank: the robot gains one uncontrollable motion

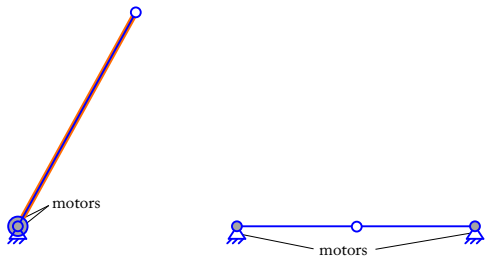

(c) Examples of singularity for $\mathbf{\Lambda}_\mathcal{L} = \nabla_{\mathbf{q}_\mathrm{pu}}\mathbf{\Phi}(\mathbf{q})$: two legs are straight and aligned

Fig. 4. Example of different types of singularities illustrated with a $\underline{R}FRF\underline{R}$ robot shown in [26] (see also Section V-A)

[5]It is well known in rigid parallel robotics that all joint configurations cannot be reached by the motors, because of robot mechanical assembly issues. Besides the active joint space boundaries, characterized by Type 2 singularities, the rigid-link parallel robots cannot be assembled anymore. Their joint space is thus constrained, unlike those of anthropomorphic serial robots.

of the workspace while the legs and platform can get an uncontrollable motion. They will be called Type 3 singularities in the rest of the paper.

4) Other types of singularities: Based on the analysis of the equations (19) and (25), other types of singularity may occur, even if in our explorations presented in Section V, we did not meet them for the moment:

- The matrix $\mathbf{\Lambda}_{\mathcal{L}} = \nabla_{\mathbf{q}_{\mathrm{pu}}} \mathbf{\Phi}(\mathbf{q})$ is not full rank: This kind of singularities will appear when some constraints equations in $\mathbf{\Phi}$ becomes redundant. By analyzing the structure of the gradient of the constraints (the interested reader could find details in Section VI of the technical report [58]), singularities of $\nabla_{\mathbf{q}_{\mathrm{pu}}} \mathbf{\Phi}(\mathbf{q})$ appear when both following conditions are satisfied:
  - Several legs are fully stretched.
  - The system of lines passing through the straight legs is degenerated (see [33], [68] for conditions of degeneracy of systems of lines).

  Thus, for the $\underline{R}FRF\underline{R}$ robot shown in [26], conditions of singularity for the matrix $\nabla_{\mathbf{q}_{\mathrm{pu}}} \mathbf{\Phi}(\mathbf{q})$ are when two legs are straight and fully aligned. We computed the gradient of the constraint for this robot in such configurations and validated that they lead to the rank deficiency of $\nabla_{\mathbf{q}_{\mathrm{pu}}} \mathbf{\Phi}(\mathbf{q})$ (Fig. 4(c)). Based on the fact that they appear only when several legs are fully stretched, such types of configurations are unlikely to appear in the context of continuum parallel robots.
- The matrix $\mathbf{U}$ is not full rank: There exists a non null motion $\Delta\mathbf{q}_{\mathrm{u}}$ leading to null motions of the motors and the platform. This is a leg singularity, similar as the ones described in [35]–[37] for rigid parallel robots.
- The matrix $\mathbf{A}$ is not full rank: There exists a non null motion $\Delta\mathbf{q}_{\mathrm{a}}$ leading to null motions of the legs and the platform. This type of singularity seems to be impossible to meet in practice.
- The matrix $\mathbf{P}$ is not full rank: There exists a non null motion $\Delta\mathbf{q}_{\mathrm{p}}$ leading to null motions of the legs and the motors. Again, this type of singularity seems to be impossible to meet in practice.

In the next section, we study the singularities of two continuum parallel robots.

V. Case studies

In this Section, we analyze the singularities and their effect for two types of continuum parallel robots: a planar robot and a spatial one. We show some preliminary computations of the stable and unstable end-effector configuration space and active joint space of these robots through the resolution of the geometrico-static model. Furthermore, we provide an analysis of the impact of singularities on these spaces and on the robots behavior in the neighborhood of the different types of singularities.

The two robots potential energy are discretized using finite differences. The Matlab codes for their models are provided as supplementary materials to this paper.

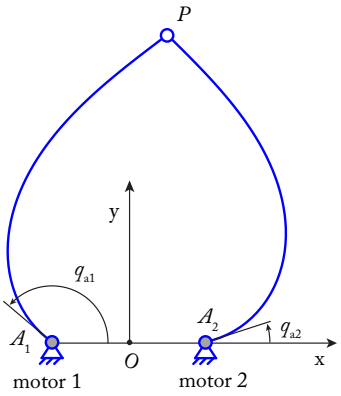

Fig. 5. Schematics of the $\underline{R}FRF\underline{R}$ robot (to scale) in the leg bluckling mode (Mode 1) tested for the computation of its end-effector configuration space.

A. The planar $\underline{R}FRF\underline{R}$ robot

In this Section, we study the continuum planar parallel robots made of two rods which has been presented in [23] (Fig. 5). It is called a $\underline{R}FRF\underline{R}$ robot because it is composed of two actuated revolute ($\underline{R}$) joints, each being mounted on the ground and attached at one extremity of a flexible rod (F). Both flexible rods are connected at their extremity through a passive revolute (R) joint. The pose $\mathbf{q}_{\mathrm{p}}$ is the coordinates of the point P, and it will be alternatively denoted by (x, y).

Parameters of the rods are: rods at rest are straight, their length L is equal to $L = 1$ m, that have circular cross-sections of radius 1 mm, and Young's moduli $E = 210$ GPa. The distance $\ell_{A_1A_2}$ between the two motors is $\ell_{A_1A_2} = 0.4$ m. No external wrenches are applied, except a force on the end-effector. The robot is modeled with the planar deformation assumption used in [23], [48], with 50 elements per legs. It has been shown in [48] that, with this number of elements, the accuracy of pose prediction is of less than 1 mm of error (for legs of 1 m) with respect to a pose computed by solving the system of constrained ODEs with a shooting method, like in [22]. Moreover, the computational time for finding a solution to the inverse or forward geometrico-static models is rather small (< 10 ms for most of configurations, whatever the initial guess, on a Pentium 4 2.70 GHz, 16 GB of RAM).

In order to investigate the impact of the singularities defined in Section IV, we first compute sets of configurations $\mathbf{q} = (\mathbf{q}_{\mathrm{a}}, \mathbf{q}_{\mathrm{p}}, \mathbf{q}_{\mathrm{u}})$ connected to an initial configuration $\mathbf{q}_0$ in which the impacts of the singularities will be studied and visualized. Aiming to display the projection of these configurations in the end-effector configuration space, an initial area of interest is discretized using a thin grid of pose vectors $\mathbf{q}_{\mathrm{p}}$ and an initial pose $\mathbf{q}_{\mathrm{p0}}$ is chosen among them. The inverse geometrico-static problem is then solved for $\mathbf{q}_{\mathrm{p0}}$ using a local search[6] with random start. This leads to an initial configuration associated with the bluckling mode for the robot legs shown in Fig. 5. Starting from this initial configuration, new configurations are computed using a flooding algorithm: A new pose vector

[6]The Levenberg-Marquardt algorithm is used, which is implemented in the *fsolve* function of Matlab, taking advantage of the computed expressions of the Jacobians of the kinemato-static model (section IV-A) in order to speed up the computation.

$\mathbf{q}_{\mathrm{p}}$ is chosen on the grid, for which no full configuration has been computed yet and which has a grid neighbor with already calculated full configuration. The inverse geometrico-static problem is then solved for this $\mathbf{q}_{\mathrm{p}}$ using the neighbor $\mathbf{q}_{\mathrm{au}}$ components as initial guess for the solver, hence having a high probability that the new configuration is connected to its neighbor in the configuration space[7]. This algorithm is particularly successful far from Type 1 singularities, where the inverse geometrico-static problem is well conditioned. It should be noted that this flooding algorithm using a static grid in the end-effector configuration space works as long as the robot is not cuspidal [72] for the tested modes of leg deformations. Its extension to cuspidal robots is possible but not in the scope of this paper.

For every configurations computed with the flooding algorithm, the inverse condition numbers $\kappa_{\mathrm{au}}^{-1}$ and $\kappa_{\mathrm{pu}}^{-1}$ of matrices $[\mathbf{A}\ \mathbf{U}]$ and $[\mathbf{P}\ \mathbf{U}]$, respectively, are calculated. Their values are displayed by color code in Fig. 6 in the robot stable and unstable end-effector configuration space when no force is applied on the end-effector. Dark blue zones are zones with bad inverse condition numbers. It should be mentioned that, in the present work, we compute condition numbers of matrices whose components have non-homogeneous units. This is valid as long as we intend to analyze the degeneracy of the corresponding matrices, and not to characterize the physical performance of the robot [73], which is not the case in this paper.

The results shows that:

- The inverse condition number $\kappa_{\mathrm{au}}^{-1}$ of $[\mathbf{A}\ \mathbf{U}]$ drops down to zero, i.e. the matrix $[\mathbf{A}\ \mathbf{U}]$ loses its rank, near the end-effector configuration space boundaries (Fig. 6(a)), as it was predicted in Section IV-B1. They correspond to Type 1 singularities.
- The zones where the inverse condition number $\kappa_{\mathrm{pu}}^{-1}$ of $[\mathbf{P}\ \mathbf{U}]$ drops down to zero, i.e. near which the matrix $[\mathbf{P}\ \mathbf{U}]$ loses its rank, appear in the middle and in the bottom of the end-effector configuration space (Fig. 6(b)). Type 2 singularities are suspected here.

Similar results, not displayed for reasons of brevity, are obtained for the same robot with a force $\mathbf{f}_0$ of 2 N along the y-direction applied at the end-effector. We also checked the value of the inverse condition number of the matrix $\mathbf{U}$ for all computed robot configurations, and it is never lower than 10^{-3}, i.e., there is no singularity of this matrix.

In Figure 7, we show the robot stable and unstable end-effector configuration space for the robot with and without a force $\mathbf{f}_0$ applied on the end-effector. In these pictures, both previously computed condition numbers are used to provide an overview of the Type 1 and Type 2 singularities in the end-effector configuration space: We highlight in red the areas where the inverse condition number of $[\mathbf{P}\ \mathbf{U}]$ is lower than $2 \cdot 10^{-5}$, i.e. near which Type 2 singularities are foreseen to be present. These red zones separate the end-effector configuration space into several connected components. When

[7]Enforcing rigorously this connectivity requires using techniques more elaborated than local search. Interval techniques can prove such connectivity, see, e.g., [69]–[71].

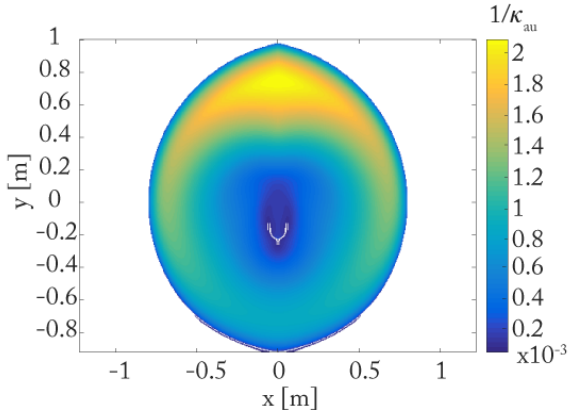

(a) Inverse condition number of $[\mathbf{A}\ \mathbf{U}]$

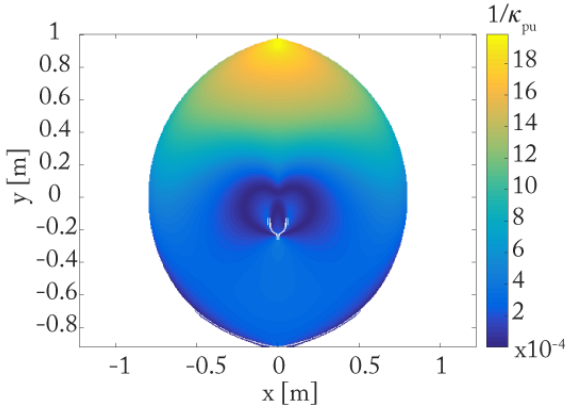

(b) Inverse condition number of $[\mathbf{P}\ \mathbf{U}]$

Fig. 6. Inverse condition numbers for the matrices $[\mathbf{A}\ \mathbf{U}]$ and $[\mathbf{P}\ \mathbf{U}]$ for the $\underline{R}FRF\underline{R}$ robot, in the leg's bluckling mode 1, when no force is applied on the end-effector.

checking the positive-definiteness of the matrix $\mathbf{H}^r$, it also appeared that the zones of low values of $\kappa_{\mathrm{pu}}^{-1}$ separate the connected components in which either all configurations are stable or unstable. This can be understood because matrix $\mathbf{H}^r$ is singular when $[\mathbf{P}\ \mathbf{U}]$ is singular, meaning that when $[\mathbf{P}\ \mathbf{U}]$ is rank-deficient, $\mathbf{H}^r$ gets a null eigenvalue. When exiting the singularity, the sign of this eigenvalue can become either positive or negative, leading to a zone in which either all configurations are stable or unstable as long as another singularity is not met. Indeed, it can be checked for instance that the zones denoted by $\mathcal{A}$, $\mathcal{B}$ and $\mathcal{C}$ in Fig. 7 correspond to zones in which there is 0, 1 and 2 negative eigenvalues of the matrix $\mathbf{H}^r$, respectively. The red areas computed using the flooding algorithm provide only an indication of the presence of Type 2 singularity curves. However, the change in the number of positive eigenvalues of the matrix $[\mathbf{P}\ \mathbf{U}]$ actually proves the existence of a curve with at least one zero eigenvalue, and therefore the presence of Type 2 singularity curves. Finally, contrary to what happens on rigid parallel robots, it should be mentioned that the location of the Type 2 singularity loci depends on the loading on the robot: This evolution can be observed in Figs. 7(a) and 7(b) for the robot with no force or with a force applied on the end-effector.

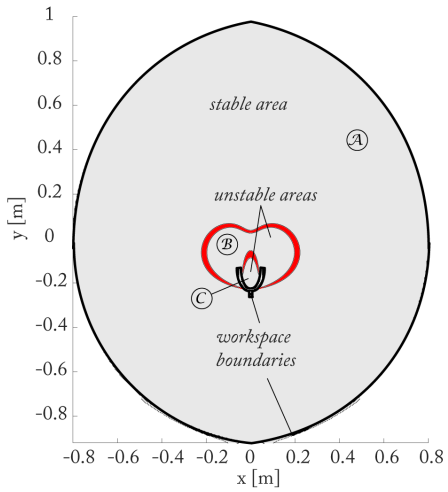

(a) with no force applied on the end-effector

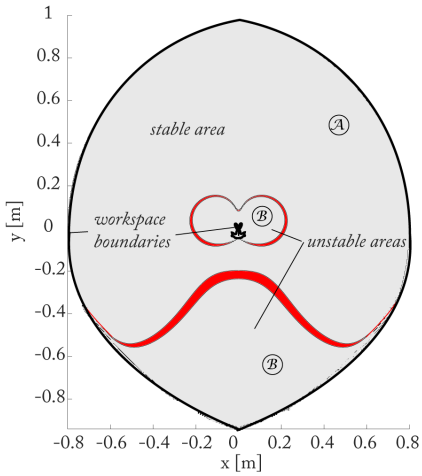

(b) with the force $\mathbf{f}_0$ applied on the end-effector

Fig. 7. Stable and unstable end-effector configuration space of the $\underline{R}FRF\underline{R}$ robot: in black bold lines: the end-effector configuration space boundaries corresponding to the singularities of the matrix $[\mathbf{A}\ \mathbf{U}]$; in red, the areas where the inverse condition number of $[\mathbf{P}\ \mathbf{U}]$ is lower than $2 \cdot 10^{-5}$, i.e. near which singularities of $[\mathbf{P}\ \mathbf{U}]$ appear.

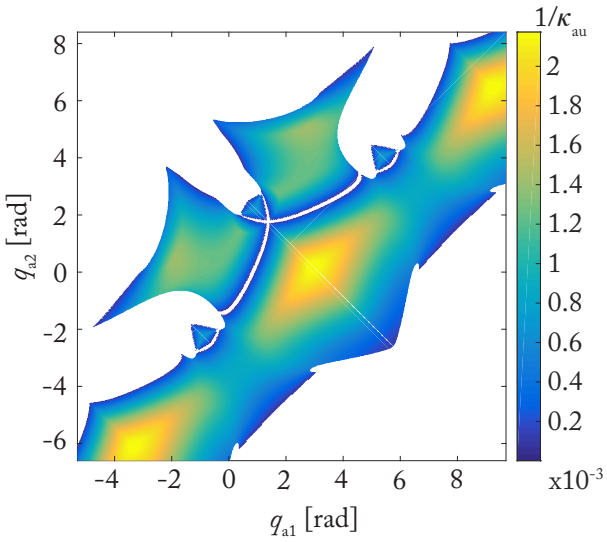

(a) Inverse condition number of $[\mathbf{A}\ \mathbf{U}]$

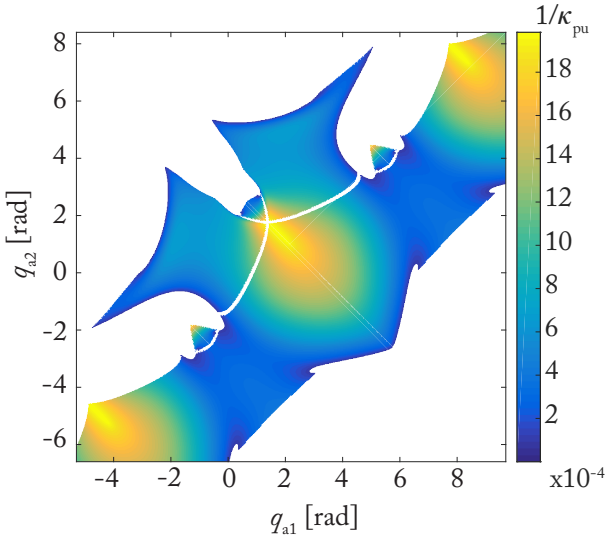

(b) Inverse condition number of $[\mathbf{P}\ \mathbf{U}]$

Fig. 8. Inverse condition numbers for the matrices $[\mathbf{A}\ \mathbf{U}]$ and $[\mathbf{P}\ \mathbf{U}]$ in the active joint space.

Then, we adapted the flooding algorithm in order to compute the robot active joint space. A grid in the $\mathbf{q}_\mathrm{a}$ space is created (instead of a grid in $\mathbf{q}_\mathrm{p}$) and the forward geometrico-static model is solved instead of the inverse one. For every configurations computed with the flooding algorithm, the inverse condition numbers κ_au^{-1} and κ_pu^{-1} of matrices $[\mathbf{A}\ \mathbf{U}]$ and $[\mathbf{P}\ \mathbf{U}]$, respectively, are calculated. Their values are displayed by color code in Fig. 8 in the robot active joint space when no force is applied on the end-effector. Dark blue zones are zones with bad inverse condition numbers.

The results shows that:

- The inverse condition number κ_pu^{-1} of $[\mathbf{P}\ \mathbf{U}]$ drops down to zero, i.e. the matrix $[\mathbf{P}\ \mathbf{U}]$ loses its rank, near the active joint space boundaries (Fig. 8(b)). They correspond to Type 2 singularities.
- The zones where the inverse condition number κ_au^{-1} of $[\mathbf{A}\ \mathbf{U}]$ drops down to zero, i.e. near which the matrix $[\mathbf{A}\ \mathbf{U}]$ loses its rank, appear in the middle and in the bottom of the end-effector configuration space (Fig. 8(a)). Type 1 singularities are suspected here.

In Figure 9, we show a part of the robot active joint space. The stability of all computed configurations is checked: all of them are stable. Again, previously computed condition numbers are used to provide an overview of the Type 1 and Type 2 singularities in the end-effector configuration space: We highlight in green the areas where the inverse condition number of $[\mathbf{A}\ \mathbf{U}]$ is lower than $2.5 \cdot 10^{-5}$, i.e. near which Type 1 singularities are foreseen to be present. These green zones separate the joint space into several components. Due to the complexity of the picture, not all components are drawn. We restrict our analysis to the components associated with the legs' modes defined in Figs. 5 and 10. This is why the joint

space is not completely bounded by Type 2 singularities.

Analyzing the configuration of the robot in each components, it appeared that the different zones correspond to different leg's bluckling modes corresponding to changes in the sign of the curvature of at least one leg: Zone 1 is associated with the robot in the leg's buckling Mode 1 (Fig. 5: legs' curvatures of opposite signs). Indeed, all configurations in Zone 1 in Fig. 9 are the configurations that we can find in Zone $\mathcal{A}$ in Fig. 7(a): Zone $\mathcal{A}$ in the end-effector space (Fig. 7(a)) corresponds to Zone 1 in the joint space (whose lower left and upper right ends are actually connected due to the 2π period therefore matching the circular geometry of Zone $\mathcal{A}$). Zone 2(a,c) with leg's buckling Mode 2 (Fig. 10(a): legs' curvatures of same signs), Zone 2(b,d) with the leg's buckling Mode 3 (Fig. 10(b)), and Zones 3(a,b,c) with the leg's buckling Mode 4 (Fig. 10(c): legs' curvatures of opposite signs, signs in opposition with Mode 1). Note that Zones 2(c,d) are not plotted in Fig. 8 for reasons of drawing clarity. Points I, I', I'' corresponds to special configurations (rotated by 180 deg from each others) where the legs are not deformed (Fig. 4(a)), i.e. their curvatures are equal to 0.

Type 1 singularities separate several zones. Boundaries $\mathcal{B}_{4(a,b,c)}$ allow to pass from legs' mode 4 to legs' mode 1 but rotated from 180 deg (Zone 1 bis in Fig. 11, which is equivalent to Zone 1 switched from 180 deg and translated from π). Other boundaries:

- $\mathcal{B}_{1(a,b)}$ separates Mode 1 from robot configurations with one inflexion point in a leg, different from modes 2 and 3 (Fig. 12(a)).
- $\mathcal{B}_{2(a,b)}$ separate Modes 2 and 3 from robot configurations with two inflexion point in a leg (Fig. 12(b)).
- $\mathcal{B}_3$ separates Modes 2 and 3 from robot configurations with one inflexion point per leg (Fig. 12(c)).

Based on these observations, we formulate the following conjecture: Type 1 singularities are related to the change of inflexion points in the legs (the only exception is between Zones 1 and 3 for which the robot has no inflexion points). However, at the time we wrote these lines, we are unable to prove this conjecture.

Thereafter, we computed the variation of the robot potential energy in the neighborhood of a configuration for which $\kappa_{\text{pu}}^{-1} = 10^{-15}$ shown in Fig. 13(a) ($x_s = 2.44 \cdot 10^{-5}$ m, $y_s = 4.965 \cdot 10^{-2}$ m when no force is applied on the end-effector). Near this singular configuration, the number of negative eigenvalues goes from zero (stable configurations) to one (unstable configurations). Therefore, $[\mathbf{P}\ \mathbf{U}]$ has one zero eigenvalue, and its nullspace has dimension one. Let us denote the projection on the end-effector configuration space (x, y) of this single nullspace vector by $\Delta_{xy} = [-.22\ .98]^T$, which is shown in Fig. 13(a). For computing the variation of energy around this configuration, we make a variation of the variables $\mathbf{q}_{\text{pu}}$ (for fixed value of $\mathbf{q}_{\text{a}}$) along two directions: The direction of the nullspace of $[\mathbf{P}\ \mathbf{U}]$ and a direction orthogonal to this nullspace that is also in the nullspace of $\nabla_{\mathbf{q}_{\text{pu}}}\mathbf{\Phi}^T$, so that both directions are tangent to the solution set of $\Phi(\mathbf{q}) = \mathbf{0}$. The results are presented in Fig. 13(b). They show that the potential energy of the robot is near an isovalue along the direction provided by Δ_{xy}, as expected.

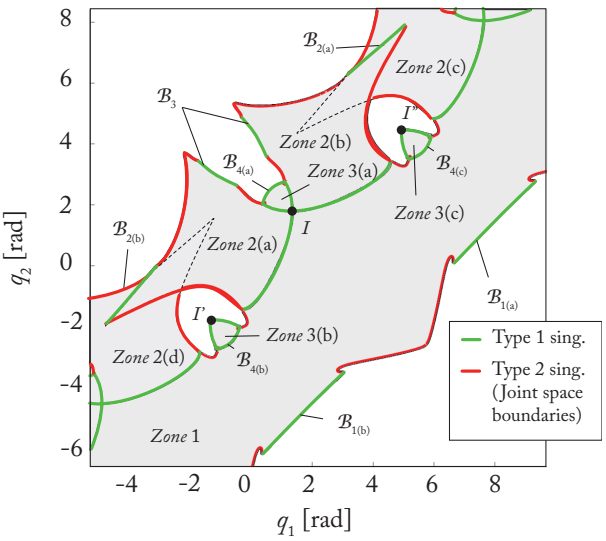

Fig. 9. Active joint space of the $\underline{R}FRF\underline{R}$ robot: in red bold lines: the joint space boundaries corresponding to the singularities of the matrix $[\mathbf{P}\ \mathbf{U}]$; in green, the areas where the inverse condition number of $[\mathbf{A}\ \mathbf{U}]$ is lower than $2.5 \cdot 10^{-5}$, i.e. near which singularities of $[\mathbf{A}\ \mathbf{U}]$ appear.

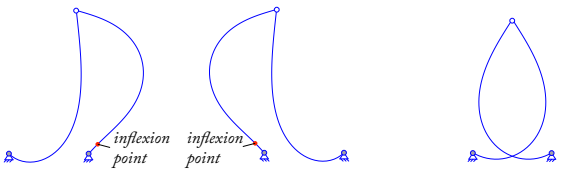

(a) Mode 2 (b) Mode 3 (c) Mode 4

Fig. 10. The leg's bluckling modes corresponding to Zones 2 and 3 in the active joint space.

We now aim at assessing more precisely the impact of this singularity and at confirming the meaningfulness of the vector Δ_{xy}, which is the potential isovalue direction. For fixed $\mathbf{q}_{\text{a}}$, we computed the external force $\mathbf{f}_{\text{p}}$ applied to the end-effector required to move it from (x_s, y_s) to a given desired close location (x, y). In order to investigate all directions, the desired location is parameterized by $(x, y) = r\,(\cos\theta, \sin\theta) + (x_s, y_s)$. In Figure 13(c), we display the vectors $\|\mathbf{f}_{\text{p}}(r, \theta)\|(\cos\theta, \sin\theta)$ for $\theta \in [0, 2\pi]$ and constant values of r ($r = 1$ cm, $r = 2$ cm and $r = 4$ cm), which allows analyzing the force amplitude needed to move the end-effector in a given direction. We also highlight the direction Δ_{xy} which characterizes the instantaneous free motion inside the singularity. It can be observed that the effort required to move the end-effector in the direction Δ_{xy} is very small compared to other directions. The ratio between the greatest and least values of the external force amplitude for a constant r is equal to 13 for $r = 1$ cm, to 7 for $r = 2$ cm and to 4 for $r = 4$ cm. As the value of r increases, we observe a decrease of the ratio, as well as a slight deviation with respect to Δ_{xy} of the desired position direction corresponding to the weakest external force. This is a consequence of the nonlinearity of the system. This overall confirms the fact that, around Type 2

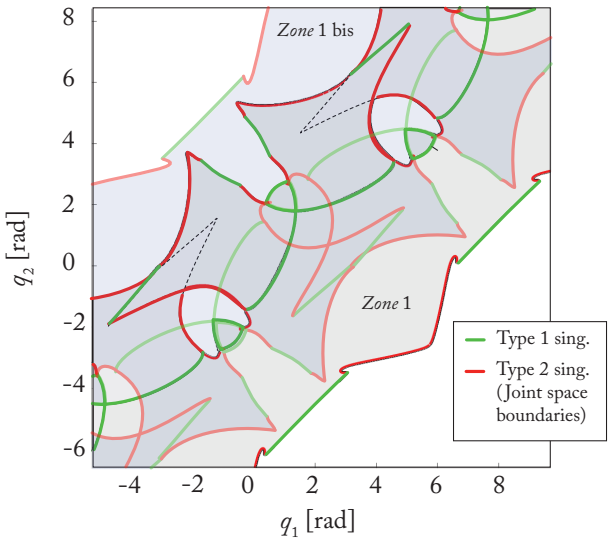

Fig. 11. Active joint space of the $\underline{R}FRF\underline{R}$ robot with some unrepresented zones from Fig. 9: Zone 1 bis corresponds to Zone 1 rotated from 180 deg. and translated from π.

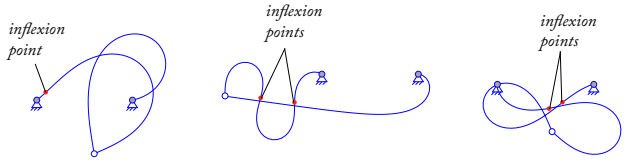

(a) when passing $\mathcal{B}_1$ (b) when passing $\mathcal{B}_3$ (c) when passing $\mathcal{B}_4$

Fig. 12. The leg's bluckling modes when passing boundaries $\mathcal{B}_1$, $\mathcal{B}_3$ and $\mathcal{B}_4$.

singularities, small external perturbations may lead to large motions of the end-effector, as described in Section IV-B2.

We also tested the effect of a small variation of the motor angles on the location of the end-effector in the stable configuration area of the end-effector configuration space when no force is applied on the end-effector (Fig. 7(a)). For all initial points marked in red in Fig. 14, associated with a initial motor joint angle value $\mathbf{q}_{\mathrm{a}0}$, we ran the forward geometrico-static model for a large number of configurations $\mathbf{q}_{\mathrm{a}}$ of the angles chosen in the interval $\mathbf{q}_{\mathrm{a}} \in [\mathbf{q}_{\mathrm{a}0} - [0.1\ 0.1]^T,\ \mathbf{q}_{\mathrm{a}0} + [0.1\ 0.1]^T]$ rad. We see that:

- Near zones where $\kappa_{\mathrm{pu}}^{-1}$ is low, then small displacements of the motor leads to large displacements of the end-effector along given directions.
- Near zones where $\kappa_{\mathrm{au}}^{-1}$ is low (near the end-effector configuration space boundaries), then the same displacement of the motor leads to almost no displacement of the end-effector along a given direction.
- There are zones near which the end-effector get a large displacement along a direction tangent to the end-effector configuration space boundary, while the displacement is very small in the orthogonal direction (bottom of the space). These are zones where both $\kappa_{\mathrm{au}}^{-1}$ and $\kappa_{\mathrm{pu}}^{-1}$ are low (see Figs. 6(a) and 6(b)), i.e. where the robot is near a singularity of both $[\mathbf{A}\ \mathbf{U}]$ and $[\mathbf{P}\ \mathbf{U}]$ (Section IV-B3).

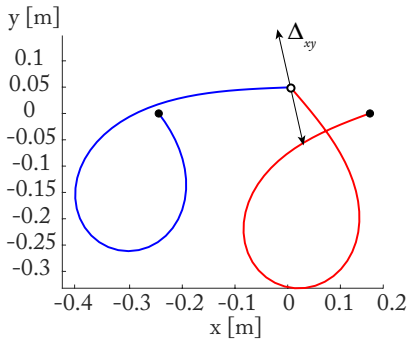

(a) Singular configuration at $x_s = 2.44 \cdot 10^{-5}$ m, $y_s = 4.965 \cdot 10^{-2}$ m, when no force is applied on the end-effector, and gained end-effector motion Δ_{xy}

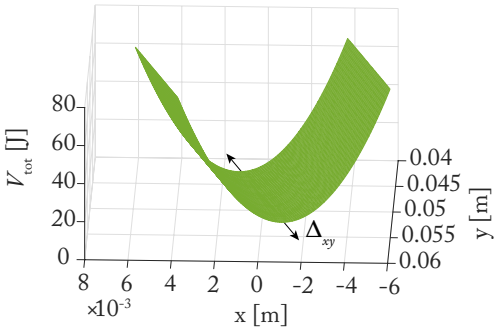

(b) Robot potential energy in the neighborhood of the configuration

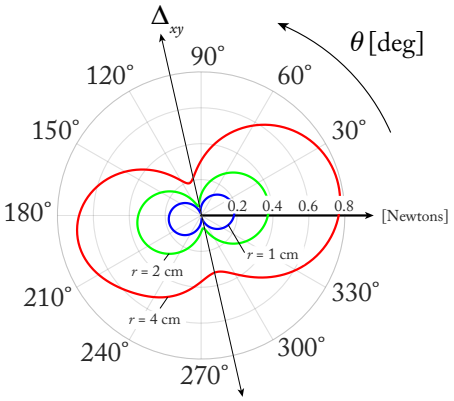

(c) Amplitude of the force required to move the end-effector at the location $(x,\ y) = r\,(\cos\theta,\ \sin\theta) - (x_s,\ y_s)$: the amplitude given as a function of θ, for constant values of r ($r = 1$ cm, $r = 2$ cm and $r = 4$ cm).

Fig. 13. Configuration leading to a singularity of $[\mathbf{P}\ \mathbf{U}]$, variation of the potential energy around this configuration, and force required to move the end-effector on circles around the singular configuration.

Finally, we analyzed the effect of a variation of a force exerted on the end-effector in the same end-effector configuration space (Fig. 7(a)). For all initial points marked in red in Fig. 15, associated with a initial motor joint angle value $\mathbf{q}_{\mathrm{a}0}$, we ran the forward geometrico-static model for many forces $\mathbf{f}_{\mathrm{p}} \in [-[0.2\ 0.2]^T,\ [0.2\ 0.2]^T]$ N. Similarly as for the variation of the actuator location, when $\kappa_{\mathrm{pu}}^{-1}$ is low, then a small force applied on the end-effector leads to its large displacement in a given direction. This is not the case for the other locations,

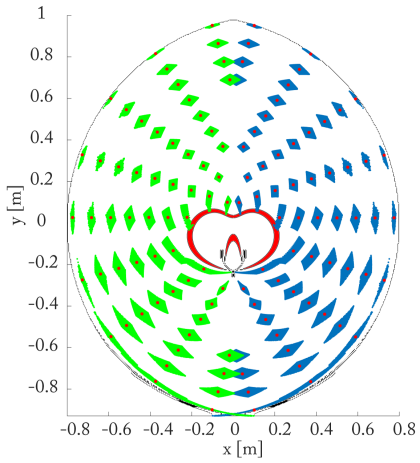

Fig. 14. Effect of a small displacement of the actuators for several initial positions (marked with the red points) for the $\underline{R}FRF\underline{R}$ robot, in the mode 1. Zones in blue and green show the displacements of the end-effector around the initial positions (different types of colors are used in order to distinguish the superposed zones).

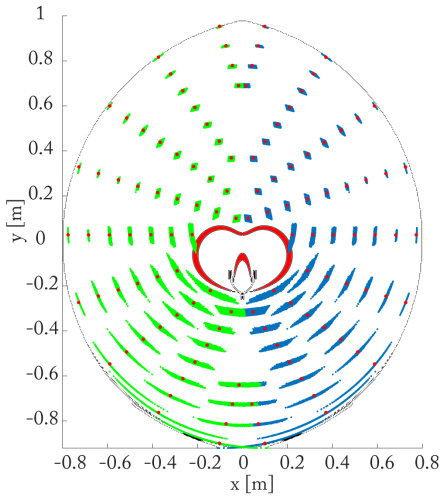

Fig. 15. Effect of the variation of the force applied at the end-effector for several initial positions (marked with the red points) for the $\underline{R}FRF\underline{R}$ robot, in the mode 1. Zones in blue and green show the displacements of the end-effector around the initial positions (different types of colors are used in order to distinguish the superposed zones).

thus showing that there is a loss of the robot stiffness in the zones where $\kappa_{\mathrm{pu}}^{-1}$ is low.

All these results show that the robot's behavior is similar to the expected behavior near the singularities of matrices $[\mathbf{A}\ \mathbf{U}]$ and $[\mathbf{P}\ \mathbf{U}]$ described in Section IV-B, which correspond respectively to Type 1 and Type 2 singularities.

B. The spatial $6-\underline{R}FS$ robot

Here, we study a continuum spatial parallel robots made of six rods (Fig. 16). The aim of this Section is to show that our work can also be applied to spatial robots. Therefore, for reason of brevity, we will not reproduce all results obtained with the previous case study, but we will focus on the study of the degeneracy of the matrices $[\mathbf{A}\ \mathbf{U}]$ and $[\mathbf{P}\ \mathbf{U}]$ in the robot end-effector configuration space.

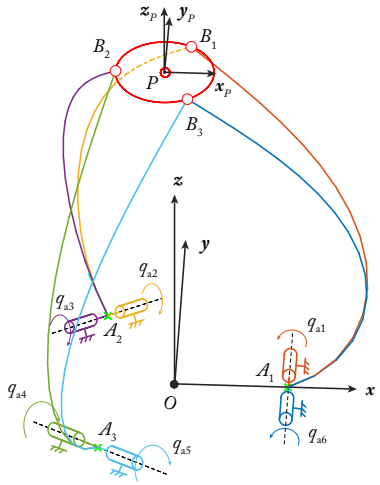

Fig. 16. Schematics of the $6-\underline{R}FS$ robot (to scale) in the leg bluckling mode tested for the computation of its end-effector configuration space.

For the studied robot, each rod is connected at the ground via an actuated revolute joint (points A_i). Its extremity is linked to a rigid moving platform via a passive spherical joint (S joint at points B_i). Using the notation introduced in [23], this robot is thus a $6-\underline{R}FS$ robot. Because the robot has six motors, it is possible to control the position and orientation of the frame $\mathcal{F}_P$: $(P,\boldsymbol{x}_P,\boldsymbol{y}_P,\boldsymbol{z}_P)$.

In the base frame $\mathcal{F}_0$: $(O,\boldsymbol{x},\boldsymbol{y},\boldsymbol{z})$, positions of points A_i are given by: $\overrightarrow{OA_i} = r_b\,[\cos\gamma_i\ \ \sin\gamma_i\ \ 0]^T$ $(i=1,2,3)$ with $r_b = 0.25$ m and $\gamma_1 = 0$, $\gamma_2 = 2\pi/3$, and $\gamma_3 = -2\pi/3$. In the platform frame $\mathcal{F}_P$, positions of points B_i are given by: $\overrightarrow{OB_i} = r_p\,[\cos\alpha_i\ \ \sin\alpha_i\ \ 0]^T$ $(i=1,2,3)$ with $r_p = 0.1$ m and $\alpha_1 = \pi/3$, $\alpha_2 = \pi$, and $\alpha_3 = -\pi/3$. Parameters of the rods are: rods at rest are straight, their length L is equal to $L = 1$ m, that have circular cross-sections of radius 1 mm, and Young's moduli $E = 210$ GPa. No external wrenches are applied. The robot is modeled with the spatial deformation assumption used in Section II. We use 30 elements per leg, which is a compromise between accuracy and computation time. In order to investigate this trade-off, Tab. I shows the pose computed for different discretizations: as expected, we can observe that when increasing the number of elements, the pose estimation tends towards an asymptotic value. There is an error of less than 3 cm on the platform frame origin estimation between the cases with 30 and 1920 elements per leg, for a robot made with legs of 1 m long, which seemed reasonable to us. Indeed, with 30 elements per leg, the computational time for each end-effector configuration space shown below (around 30,000 configurations computed per picture) was already between 6 and 8 hours on our Pentium 4 2.70 GHz, 16 GB of RAM. Therefore, we decided to keep this number of elements which seemed to us a good trade off between computational time and model accuracy. Improving the trade-off between the computation time and the accuracy of pose estimation by using a better discretization process is not in the scope of this paper.

As previously, in order to investigate the impact of the singularities defined in Section IV, we compute sets of configurations $\mathbf{q} = (\mathbf{q}_{\mathrm{a}}, \mathbf{q}_{\mathrm{p}}, \mathbf{q}_{\mathrm{u}})$ connected to an initial configuration

TABLE I
PLATFORM POSE COMPUTED FOR DIFFERENT NUMBERS N_i OF ELEMENTS PER LEG (N_i IS IDENTICAL FOR EACH LEG), WHEN THE ACTUATORS ARE AT $\mathbf{q}_a = [54, \ -17, \ 74, \ -30, \ 22, \ 3]$ DEG.

N_i	x [mm]	y [mm]	z [mm]	ϕ [deg]	θ [deg]	ψ [deg]
15	-16.25	3.92	549.08	48.86	31.63	-2.50
30	-23.26	14.64	567.65	51.56	31.75	-2.55
60	-26.89	21.20	578.73	52.42	31.84	-2.52
120	-28.64	23.80	584.73	52.75	31.89	-2.51
240	-29.49	24.94	587.84	52.89	31.91	-2.51
480	-29.91	25.47	589.43	52.95	31.92	-2.51
960	-30.12	25.72	590.23	52.98	31.92	-2.51
1920	-30.15	25.80	590.64	52.98	31.92	-2.51

$\mathbf{q}_0$ and we display the projection of these configurations in the end-effector configuration space. The previous flooding algorithm is used, but for reasons of computation cost, we forced it to compute only configurations in xy-slices of the end-effector configuration space, i.e. we constrained the platform to keep constant values for its altitude and orientation.

For every configurations computed with the previous flooding algorithm, the inverse condition numbers κ_{au}^{-1} and κ_{pu}^{-1} of matrices $[\mathbf{A}\ \mathbf{U}]$ and $[\mathbf{P}\ \mathbf{U}]$, respectively, are calculated. Their values are displayed by color code in Fig. 17 in the robot end-effector configuration space, for platform altitude and orientation defined by: $z = 0.55$ m, $\phi = \pi/4$ rad, $\theta = \pi/6$ rad, and $\psi = 0$ rad (these three angles are defined in the ZYZ Euler-angle convention). Dark blue zones are zones with bad inverse condition numbers.

As for the previous robot, the results shows that:

- The inverse condition number κ_{au}^{-1} of $[\mathbf{A}\ \mathbf{U}]$ drops down to zero, i.e. the matrix $[\mathbf{A}\ \mathbf{U}]$ loses its rank, near the end-effector configuration space boundaries (Fig. 17(a)), as it was predicted in Section IV-B1. They correspond to Type 1 singularities.
- The zones where the inverse condition number κ_{pu}^{-1} of $[\mathbf{P}\ \mathbf{U}]$ drops down to zero, i.e. near which the matrix $[\mathbf{P}\ \mathbf{U}]$ loses its rank, appear in the middle and in the bottom of the end-effector configuration space (Fig. 17(b)). Type 2 singularities are suspected here.

Similar results, not displayed for reasons of brevity, are obtained for the same robot for another platform altitude and orientation defined by: $z = 0.55$ m, $\phi = \pi/3$ rad, $\theta = \pi/12$ rad, and $\psi = 0$ rad, or for a wrench ($f_x = 0.5$ N, $f_y = 0.1$ N, $f_z = -0.2$ N, $m_x = 0.1$ Nm, $m_y = -0.1$ Nm, $m_z = 0.05$ Nm) applied at the platform frame origin.

In Figure 18, we show the xy-slices of the end-effector configuration space for the two previously mentioned altitudes and orientations of the platform, with and without external wrench applied on the robot. In these pictures, both previously computed condition numbers are used to provide an overview of the Type 1 and Type 2 singularities in the end-effector configuration space: We highlight in red the areas where the inverse condition number of $[\mathbf{P}\ \mathbf{U}]$ is lower than $2 \cdot 10^{-5}$, i.e. near which Type 2 singularities are foreseen to be present. As previously, these red zones separate the end-effector configuration space into several connected components. When checking the positive-definiteness of the matrix $\mathbf{H}^r$, it appeared that the

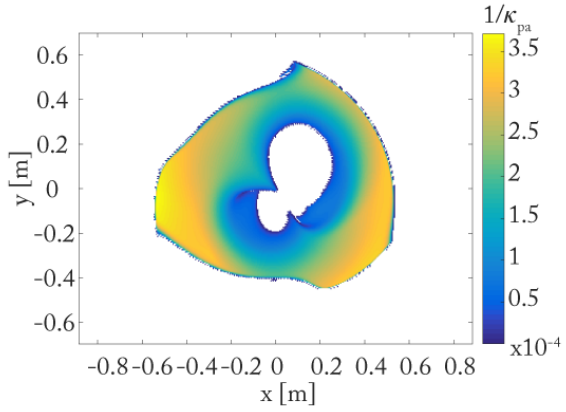

(a) Inverse condition number of $[\mathbf{A}\ \mathbf{U}]$

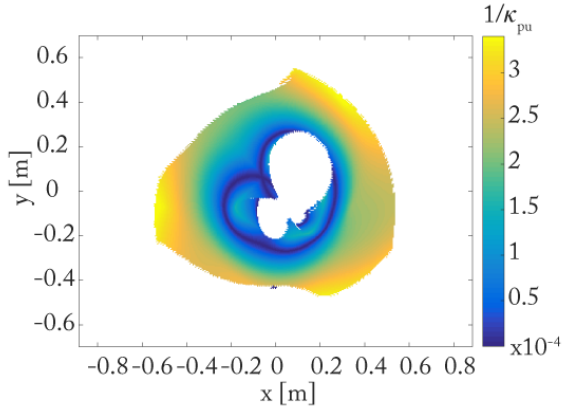

(b) Inverse condition number of $[\mathbf{P}\ \mathbf{U}]$

Fig. 17. Inverse condition numbers for the matrices $[\mathbf{A}\ \mathbf{U}]$ and $[\mathbf{P}\ \mathbf{U}]$ for the $6-\underline{R}FS$ robot in the xy-slice of the end-effector configuration space obtained for platform altitude and orientation defined by: $z = 0.55$ m, $\phi = \pi/4$ rad, $\theta = \pi/6$ rad, and $\psi = 0$ rad (these three angles are defined in the ZYZ Euler-angle convention).

zones of low values of κ_{pu}^{-1} separate the connected components in which either all configurations are stable or unstable. Again, although the red areas computed using the flooding algorithm provide only an indication of the presence of Type 2 singularity curves, the change in the number of positive eigenvalues of the matrix $[\mathbf{P}\ \mathbf{U}]$ actually proves their existence.

We remark again in Figs. 18(a) and 18(b) that the location of the singularity loci, for a fixed platform orientation, depends on the value of the external wrenches applied on the robot.

Finally, we replayed the previous simulations for obtaining the robot orientation end-effector configuration space. An illustration of this end-effector configuration space is shown in Fig. 19 (slice $\phi\theta$ of the orientation end-effector configuration space at $\psi = 0$ rad, using the ZYZ Euler-angle convention, for a fixed platform frame origin). Again, the existence of different zones, separated by low values of the condition number of $[\mathbf{P}\ \mathbf{U}]$, and with differences in the number of positive eigenvalues of the matrix $[\mathbf{P}\ \mathbf{U}]$, proves the existence of Type 2 singularities.

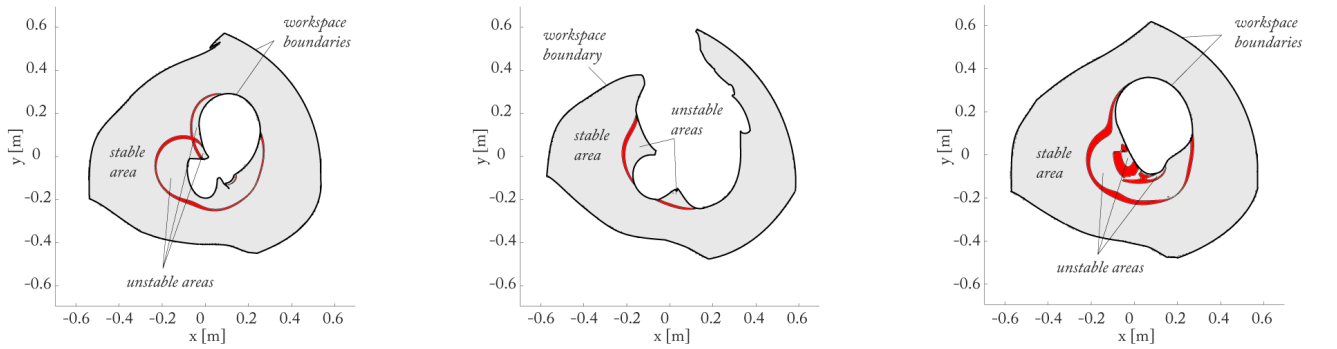

(a) for $z = 0.55$ m, $\phi = \pi/4$ rad, $\theta = \pi/6$ rad, and $\psi = 0$ rad, no external wrench.

(b) for $z = 0.55$ m, $\phi = \pi/4$ rad, $\theta = \pi/6$ rad, and $\psi = 0$ rad, external wrench ($f_x = 0.5$ N, $f_y = 0.1$ N, $f_z = -0.2$ N, $m_x = 0.1$ Nm, $m_y = -0.1$ Nm, $m_z = 0.05$ Nm) applied at point P.

(c) for $z = 0.55$ m, $\phi = \pi/3$ rad, $\theta = \pi/12$ rad, and $\psi = 0$ rad, no external wrench.

Fig. 18. xy-slice of the end-effector configuration space obtained for different platform altitudes and orientations or external wrenches; angles are defined in the ZYZ Euler-angle convention; in black bold lines: the end-effector configuration space boundaries corresponding to the singularities of the matrix $[\mathbf{A}\ \mathbf{U}]$; in red, the areas where the inverse condition number of $[\mathbf{P}\ \mathbf{U}]$ is lower than $2 \cdot 10^{-5}$, i.e. near which singularities of $[\mathbf{P}\ \mathbf{U}]$ appear.

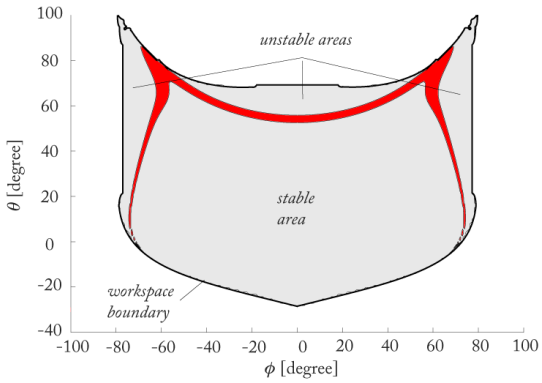

Fig. 19. Slice $\phi\theta$ of the orientation end-effector configuration space at $\psi = 0$ rad (these three angles are defined in the ZYZ Euler-angle convention), platform frame origin located at $x = -0.3$ m, $y = 0$ m, $z = 0.55$ m; in black bold lines: the end-effector configuration space boundaries corresponding to the singularities of the matrix $[\mathbf{A}\ \mathbf{U}]$; in red, the areas where the inverse condition number of $[\mathbf{P}\ \mathbf{U}]$ is lower than $2 \cdot 10^{-5}$, i.e. near which singularities of $[\mathbf{P}\ \mathbf{U}]$ appear.

VI. Conclusions

In this paper, we have defined the singularity conditions for generic continuum parallel robots. Based on this definition, we provided a straightforward interpretation of the phenomena occurring in singularities. We have classified these singularities as follows: Type 1, Type 2, Type 3 and legs' singularities. More specifically, Type 1 singularities correspond to the impossibility of the robot to move along given directions, thus defining the workspace boundaries. We have conjectured a relationship between Type 1 singularities and changes in the legs buckling modes, although we were not able to prove it. Type 2 singularities corresponds to gained motions of the robot for fixed motor positions, thus defining the active joint space boundaries. We proved that these singularities appear when the robot potential energy has a local isovalue. This has been shown to imply that Type 2 singularities separate the end-effector configuration space into different areas, some of them containing only stable configurations, the other containing only unstable ones. Moreover, on Type 2 singularity, the robot can freely move along a given direction without any constraint under the action of small perturbations. Type 3 singularities are a combination of both Type 1 and Type 2 singularities, while leg's singularities lead to free legs' motions for fixed positions of both motors and end-effector.

We illustrated the singularity phenomena and their effects by simulations performed with two different continuum parallel robots: a planar $\underline{R}FR\underline{FR}$ robot, and a spatial $6-\underline{R}FS$ robot.

Future works will concern the usage of the analytical expressions of the kinemato-static model for computing the singularity loci of continuum parallel robots. Especially, we believe that it is possible to optimize the design parameters of the continuum parallel robots in order to obtain robots with the largest singularity-free workspace as possible, and even, to design robots without any singularity. We also expect to define the singularities by the direct analysis of the system of ODEs characterizing the geometrico-static behavior of the continuum parallel robots. Finally, we will devote some efforts on the improvement of our flooding algorithm for the workspace computation, which, in the present version, is very sensitive to the tuning of some parameters (solvers used, maximal number of allowed iterations, etc.), leading to some potential issues of changes in the robot leg's mode between two neighboring configurations, especially near singularities. The use of certified numerical algorithms, based on interval analysis, will be explored for solving these issues.

Appendix

A. Stability analysis of the solution $\mathbf{q}^*_{\mathrm{pu}}$

The analysis of the stability based on the criterion (17) comes from the following explanation. Taking the second-

order approximation of the Lagrangian function $\mathcal{L} = V_{\text{tot}} + \mathbf{\Phi}^T\boldsymbol{\lambda}$ for a fixed value of $\mathbf{q}_\text{a}$, we have

$$\begin{aligned}
&\mathcal{L}(\mathbf{q}_\text{a}, \mathbf{q}^*_\text{pu} + \Delta\mathbf{q}_\text{pu}, \boldsymbol{\lambda}^* + \Delta\boldsymbol{\lambda}) \approx \mathcal{L}(\mathbf{q}_\text{a}, \mathbf{q}^*_\text{pu}, \boldsymbol{\lambda}^*) + \\
&\begin{bmatrix}\Delta\mathbf{q}_\text{pu}\\ \Delta\boldsymbol{\lambda}\end{bmatrix}^T \begin{bmatrix}\nabla_{\mathbf{q}_\text{pu}}\mathcal{L}(\mathbf{q}_\text{a}, \mathbf{q}^*_\text{pu}, \boldsymbol{\lambda}^*)\\ \nabla_{\boldsymbol{\lambda}}\mathcal{L}(\mathbf{q}_\text{a}, \mathbf{q}^*_\text{pu}, \boldsymbol{\lambda}^*)\end{bmatrix} + \frac{1}{2}\begin{bmatrix}\Delta\mathbf{q}_\text{pu}\\ \Delta\boldsymbol{\lambda}\end{bmatrix}^T \cdot \\
&\begin{bmatrix}D_{\mathbf{q}_\text{pu}}\nabla_{\mathbf{q}_\text{pu}}\mathcal{L}(\mathbf{q}_\text{a}, \mathbf{q}^*_\text{pu}, \boldsymbol{\lambda}^*) & D_{\boldsymbol{\lambda}}\nabla_{\mathbf{q}_\text{pu}}\mathcal{L}(\mathbf{q}_\text{a}, \mathbf{q}^*_\text{pu}, \boldsymbol{\lambda}^*)\\ D_{\mathbf{q}_\text{pu}}\nabla_{\boldsymbol{\lambda}}\mathcal{L}(\mathbf{q}_\text{a}, \mathbf{q}^*_\text{pu}, \boldsymbol{\lambda}^*) & \mathbf{0}\end{bmatrix}\begin{bmatrix}\Delta\mathbf{q}_\text{pu}\\ \Delta\boldsymbol{\lambda}\end{bmatrix} \\
&= \mathcal{L}(\mathbf{q}_\text{a}, \mathbf{q}^*_\text{pu}, \boldsymbol{\lambda}^*) + \begin{bmatrix}\Delta\mathbf{q}_\text{pu}\\ \Delta\boldsymbol{\lambda}\end{bmatrix}^T \begin{bmatrix}\nabla_{\mathbf{q}_\text{pu}}\mathcal{L}(\mathbf{q}_\text{a}, \mathbf{q}^*_\text{pu}, \boldsymbol{\lambda}^*)\\ \mathbf{\Phi}^T(\mathbf{q}_\text{a}, \mathbf{q}^*_\text{pu})\end{bmatrix} + \\
&\frac{1}{2}\begin{bmatrix}\Delta\mathbf{q}_\text{pu}\\ \Delta\boldsymbol{\lambda}\end{bmatrix}^T \begin{bmatrix}\mathbf{H}(\mathbf{q}_\text{a}, \mathbf{q}^*_\text{pu}, \boldsymbol{\lambda}^*) & \nabla_{\mathbf{q}_\text{pu}}\mathbf{\Phi}(\mathbf{q}_\text{a}, \mathbf{q}^*_\text{pu})\\ \nabla_{\mathbf{q}_\text{pu}}\mathbf{\Phi}(\mathbf{q}_\text{a}, \mathbf{q}^*_\text{pu})^T & \mathbf{0}\end{bmatrix}\begin{bmatrix}\Delta\mathbf{q}_\text{pu}\\ \Delta\boldsymbol{\lambda}\end{bmatrix}
\end{aligned} \tag{31}$$

If $\mathbf{q}^*_\text{pu}$ and $\boldsymbol{\lambda}^*$ are solutions of (14) and (15), then $\nabla_{\mathbf{q}_\text{pu}}\mathcal{L}(\mathbf{q}_\text{a}, \mathbf{q}^*_\text{pu}, \boldsymbol{\lambda}^*) = \mathbf{0}$ and $\mathbf{\Phi}(\mathbf{q}_\text{a}, \mathbf{q}^*_\text{pu}) = \mathbf{0}$. Thus, Eq. (31) can be rewritten as:

$$\begin{aligned}
&\mathcal{L}(\mathbf{q}_\text{a}, \mathbf{q}^*_\text{pu} + \Delta\mathbf{q}_\text{pu}, \boldsymbol{\lambda}^* + \Delta\boldsymbol{\lambda}) \approx \mathcal{L}(\mathbf{q}_\text{a}, \mathbf{q}^*_\text{pu}, \boldsymbol{\lambda}^*) + \\
&\frac{1}{2}\Delta\mathbf{q}_\text{pu}{}^T\mathbf{H}(\mathbf{q}_\text{a}, \mathbf{q}^*_\text{pu}, \boldsymbol{\lambda}^*)\Delta\mathbf{q}_\text{pu} + \\
&\Delta\boldsymbol{\lambda}^T\nabla_{\mathbf{q}_\text{pu}}\mathbf{\Phi}(\mathbf{q}_\text{a}, \mathbf{q}^*_\text{pu})^T\Delta\mathbf{q}_\text{pu}
\end{aligned} \tag{32}$$

Because $\mathbf{\Phi}(\mathbf{q}_\text{a}, \mathbf{q}^*_\text{pu}) = \mathbf{0}$, all small variations $\Delta\mathbf{q}_\text{pu}$ of $\mathbf{q}_\text{pu}$ are contained in the nullspace of $\nabla_{\mathbf{q}_\text{pu}}\mathbf{\Phi}(\mathbf{q}_\text{a}, \mathbf{q}^*_\text{pu})^T$, i.e. $\nabla_{\mathbf{q}_\text{pu}}\mathbf{\Phi}(\mathbf{q}_\text{a}, \mathbf{q}^*_\text{pu})^T\Delta\mathbf{q}_\text{pu} = \mathbf{0}$, meaning that:

$$\begin{aligned}
&\mathcal{L}(\mathbf{q}_\text{a}, \mathbf{q}^*_\text{pu} + \Delta\mathbf{q}_\text{pu}, \boldsymbol{\lambda}^* + \Delta\boldsymbol{\lambda}) \approx \mathcal{L}(\mathbf{q}_\text{a}, \mathbf{q}^*_\text{pu}, \boldsymbol{\lambda}^*) + \\
&\frac{1}{2}\Delta\mathbf{q}_\text{pu}{}^T\mathbf{H}(\mathbf{q}_\text{a}, \mathbf{q}^*_\text{pu}, \boldsymbol{\lambda}^*)\Delta\mathbf{q}_\text{pu}
\end{aligned} \tag{33}$$

If $(\mathbf{q}_\text{a}, \mathbf{q}^*_\text{pu}, \boldsymbol{\lambda}^*)$ is solution to the equations (14) and (15), then $\mathbf{\Phi}(\mathbf{q}_\text{a}, \mathbf{q}^*_\text{pu}) = \mathbf{0}$ and $\mathcal{L}(\mathbf{q}_\text{a}, \mathbf{q}^*_\text{pu}, \boldsymbol{\lambda}^*) = V_\text{tot}(\mathbf{q}_\text{a}, \mathbf{q}^*_\text{pu})$:

$$\begin{aligned}
&\mathcal{L}(\mathbf{q}_\text{a}, \mathbf{q}^*_\text{pu} + \Delta\mathbf{q}_\text{pu}, \boldsymbol{\lambda}^* + \Delta\boldsymbol{\lambda}) \approx V_\text{tot}(\mathbf{q}_\text{a}, \mathbf{q}^*_\text{pu}) + \\
&\frac{1}{2}\Delta\mathbf{q}_\text{pu}{}^T\mathbf{H}(\mathbf{q}_\text{a}, \mathbf{q}^*_\text{pu}, \boldsymbol{\lambda}^*)\Delta\mathbf{q}_\text{pu}
\end{aligned} \tag{34}$$

Moreover, we see that the expression (33) is independent of the variation $\Delta\boldsymbol{\lambda}$. Thus $\mathcal{L}(\mathbf{q}_\text{a}, \mathbf{q}^*_\text{pu} + \Delta\mathbf{q}_\text{pu}, \boldsymbol{\lambda}^* + \Delta\boldsymbol{\lambda}) = \mathcal{L}(\mathbf{q}_\text{a}, \mathbf{q}^*_\text{pu} + \Delta\mathbf{q}_\text{pu}, \boldsymbol{\lambda}^*)$. Finally, because the only possible variations $\Delta\mathbf{q}_\text{pu}$ are those contained in the nullspace $\mathbf{Z}$ of $\nabla_{\mathbf{q}_\text{pu}}\mathbf{\Phi}(\mathbf{q}_\text{a}, \mathbf{q}^*_\text{pu})^T$, i.e. those admissible by the real system keeping the constraint equations $\mathbf{\Phi}(\mathbf{q}_\text{a}, \mathbf{q}^*_\text{pu} + \Delta\mathbf{q}_\text{pu}) = \mathbf{0}$ true, it means that

$$\mathcal{L}(\mathbf{q}_\text{a}, \mathbf{q}^*_\text{pu} + \Delta\mathbf{q}_\text{pu}, \boldsymbol{\lambda}^*) = V_\text{tot}(\mathbf{q}_\text{a}, \mathbf{q}^*_\text{pu} + \Delta\mathbf{q}_\text{pu}) \tag{35}$$

If $\Delta\mathbf{q}_\text{pu}$ is contained in the nullspace $\mathbf{Z}$ of $\nabla_{\mathbf{q}_\text{pu}}\mathbf{\Phi}(\mathbf{q}_\text{a}, \mathbf{q}^*_\text{pu})^T$, this also means that all $\Delta\mathbf{q}_\text{pu}$ can be written as $\Delta\mathbf{q}_\text{pu} = \mathbf{Z}\Delta\mathbf{v}$, with $\Delta\mathbf{v}$ a vector image of the variation of the true generalized coordinates of the system. Thus,

$$\begin{aligned}
&V_\text{tot}(\mathbf{q}_\text{a}, \mathbf{q}^*_\text{pu} + \Delta\mathbf{q}_\text{pu}) = V_\text{tot}(\mathbf{q}_\text{a}, \mathbf{q}^*_\text{pu} + \mathbf{Z}\Delta\mathbf{v}) \\
&\approx V_\text{tot}(\mathbf{q}_\text{a}, \mathbf{q}^*_\text{pu}) + \frac{1}{2}\Delta\mathbf{v}^T\mathbf{Z}^T\mathbf{H}(\mathbf{q}_\text{a}, \mathbf{q}^*_\text{pu}, \boldsymbol{\lambda}^*)\mathbf{Z}\Delta\mathbf{v} \\
&= V_\text{tot}(\mathbf{q}_\text{a}, \mathbf{q}^*_\text{pu}) + \frac{1}{2}\Delta\mathbf{v}^T\mathbf{H}^r(\mathbf{q}_\text{a}, \mathbf{q}^*_\text{pu}, \boldsymbol{\lambda}^*)\Delta\mathbf{v}
\end{aligned} \tag{36}$$

and $\mathbf{H}^r$ is the Hessian of the potential energy for a set of true generalized coordinates.

B. Expression of the kinemato-static model involving external wrenches

The dependence of the potential energy with respect to the constant wrenches applied to the robot was not displayed explicitly in Section III. With this explicit dependence, Equation (14) defining the geometrico-static model becomes

$$\nabla_{\mathbf{q}_\text{pu}}V_\text{tot}(\mathbf{q}, \mathbf{w}) + \nabla_{\mathbf{q}_\text{pu}}\mathbf{\Phi}(\mathbf{q})\,\boldsymbol{\lambda} = \mathbf{0}. \tag{37}$$

Jacobian matrices $\mathbf{A}$, $\mathbf{P}$ and $\mathbf{U}$ then depends on $\mathbf{w}$ as well. An additional Jacobian matrix

$$\mathbf{W} = \begin{bmatrix}\mathbf{Z}^T D_\mathbf{w}\nabla_{\mathbf{q}_\text{pu}}\mathcal{L}\\ \mathbf{0}\end{bmatrix} \tag{38}$$

has to be introduced in order to take into account the wrench variations in the kinemato-static model. Then (25) becomes

$$\mathbf{A}\,\Delta\mathbf{q}_\text{a} + \mathbf{P}\,\Delta\mathbf{q}_\text{p} + \mathbf{U}\,\Delta\mathbf{q}_\text{u} + \mathbf{W}\Delta\mathbf{w} = \mathbf{0}. \tag{39}$$

The forward and inverse kinemato-static problems have respectively the following solutions:

$$\begin{bmatrix}\Delta\mathbf{q}_\text{p}\\ \Delta\mathbf{q}_\text{u}\end{bmatrix} = -\begin{bmatrix}\mathbf{P} & \mathbf{U}\end{bmatrix}^{-1}(\mathbf{A}\;\Delta\mathbf{q}_\text{a} + \mathbf{W}\Delta\mathbf{w}). \tag{40}$$

$$\begin{bmatrix}\Delta\mathbf{q}_\text{a}\\ \Delta\mathbf{q}_\text{u}\end{bmatrix} = -\begin{bmatrix}\mathbf{A} & \mathbf{U}\end{bmatrix}^{-1}(\mathbf{P}\;\Delta\mathbf{q}_\text{p} + \mathbf{W}\Delta\mathbf{w}). \tag{41}$$

This leads to the same singularity definitions and interpretations as previously.

Additionally, the matrix $\mathbf{C} = \begin{bmatrix}\mathbf{P} & \mathbf{U}\end{bmatrix}^{-1}\mathbf{W}$ involved in (40) can be related to the compliance matrix provided in [22]. When considering only variations of the external wrenches $\mathbf{w}_\text{p}$ applied to the platform only, i.e. $\Delta\mathbf{w} = \Delta\mathbf{w}_\text{p}$, as it was the case for the definition of the compliance matrix in [22], then the matrix $\mathbf{W}$ takes the following form (assuming that vector $\mathbf{q}_\text{pu}$ is ordered such that $\mathbf{q}_\text{pu} = [\mathbf{p}_\text{p}^T\ \mathbf{h}_\text{p}^T\ \mathbf{h}^T]^T$):

$$\mathbf{W} = -\begin{bmatrix}\left(\mathbf{Z}^T\begin{bmatrix}\mathbf{1}_3 & \mathbf{0}\\ \mathbf{0} & \mathbf{0}\\ \mathbf{0} & \mathbf{0}\end{bmatrix}\right)\\ \mathbf{0}\end{bmatrix} \tag{42}$$

Then, $\mathbf{W}$ is rank deficient if and only if the product $\mathbf{Z}^T\begin{bmatrix}\mathbf{1}_3 & \mathbf{0}\\ \mathbf{0} & \mathbf{0}\\ \mathbf{0} & \mathbf{0}\end{bmatrix}$ is not full rank, i.e. if it exists a vector $\mathbf{t}$ of the form

$$\mathbf{t} = \begin{bmatrix}\mathbf{1}_3 & \mathbf{0}\\ \mathbf{0} & \mathbf{0}\\ \mathbf{0} & \mathbf{0}\end{bmatrix}\begin{bmatrix}\boldsymbol{\alpha}_1\\ \boldsymbol{\alpha}_2\end{bmatrix} = \begin{bmatrix}\mathbf{1}_3\boldsymbol{\alpha}_1\\ \mathbf{0}\\ \mathbf{0}\end{bmatrix}, \tag{43}$$

for given values of the three dimensional vector $\boldsymbol{\alpha}_1$ defined such that $\boldsymbol{\alpha}_1 \neq 0$, for which that $\mathbf{Z}^T\mathbf{t} = \mathbf{0}$.

$\mathbf{Z}$ being the nullspace of the transpose of the gradient $\nabla_{\mathbf{q}_\text{pu}}\mathbf{\Phi}(\mathbf{q})$, i.e. $\nabla_{\mathbf{q}_\text{pu}}\mathbf{\Phi}(\mathbf{q})^T\mathbf{Z} = \mathbf{0}$ and also $\mathbf{Z}^T\nabla_{\mathbf{q}_\text{pu}}\mathbf{\Phi}(\mathbf{q}) = \mathbf{0}$, this would mean that $\mathbf{t}$ must span the image of $\nabla_{\mathbf{q}_\text{pu}}\mathbf{\Phi}(\mathbf{q})$, i.e. that we must have

$$\begin{aligned}
\mathbf{t} &= \begin{bmatrix}\mathbf{1}_3\boldsymbol{\alpha}_1\\ \mathbf{0}\\ \mathbf{0}\end{bmatrix} = \nabla_{\mathbf{q}_\text{pu}}\mathbf{\Phi}(\mathbf{q})\mathbf{u} \\
&= \begin{bmatrix}\nabla_{\mathbf{p}_\text{p}}\mathbf{\Phi}(\mathbf{q})\\ \nabla_{\mathbf{h}_\text{p}}\mathbf{\Phi}(\mathbf{q})\\ \nabla_{\mathbf{h}}\mathbf{\Phi}(\mathbf{q})\end{bmatrix}\mathbf{u} = \begin{bmatrix}\nabla_{\mathbf{p}_\text{p}}\mathbf{\Phi}(\mathbf{q})\mathbf{u}\\ \nabla_{\mathbf{h}_\text{p}}\mathbf{\Phi}(\mathbf{q})\mathbf{u}\\ \nabla_{\mathbf{h}}\mathbf{\Phi}(\mathbf{q})\mathbf{u}\end{bmatrix}
\end{aligned} \tag{44}$$

for a given non null vector $\mathbf{u}$. The condition $\nabla_{\mathbf{h}}\mathbf{\Phi}(\mathbf{q})\mathbf{u} = \mathbf{0}$ means that $\nabla_{\mathbf{h}}\mathbf{\Phi}(\mathbf{q})$ must be rank deficient. However, as shown in the Section VI of [58], this can never appear, except when several legs are fully extended, which are uninteresting configurations in practice.

As a result, $\mathbf{W}$ can never lose its rank and the condition number associated with the matrix $\mathbf{C}$ goes to infinity only when matrix $\begin{bmatrix}\mathbf{P} & \mathbf{U}\end{bmatrix}$ degenerates. Therefore, the degeneracy of the compliance matrix found in [22] is thus a Type 2 singularity. A similar analysis leads to the conclusion that the singular configurations found in [26], which are associated with the degeneracy of the stiffness matrix that involves $\begin{bmatrix}\mathbf{P} & \mathbf{U}\end{bmatrix}$, are also Type 2 singularities. Note finally that computing the variation $\Delta\mathbf{w}$ for known variations $\Delta\mathbf{q}$ has little interest in practice. Thus, computing the associated singularities for wrenches other than those applied on the platform is out of the scope of this paper.

ACKNOWLEDGMENT

The authors would like to thank the unknown reviewers for their valuable remarks that greatly contributed to the improvement of the paper.

REFERENCES

[1] S. Hirose and M. Mori, "Biologically inspired snake-like robots," in *Proceedings of the 2004 IEEE International Conference on Robotics and Biomimetics (ROBIO2004)*, Shenyang, China, 2004.

[2] D. Trivedi, C. Rahn, W. Kierband, and I. Walker, "Soft robotics: Biological inspiration, state of the art, and future research," *Applied Bionics and Biomechanics*, vol. 5, no. 3, pp. 99–117, 2008.

[3] J. Burgner-Kahrs, D. Rucker, and H. Choset, "Continuum robots for medical applications: A survey," *IEEE Transactions on Robotics*, vol. 31, no. 6, pp. 1261–1280, 2015.

[4] D. Camarillo, C. Milne, C. Carlson, M. Zinn, and J. Salisbury, "Mechanics modeling of tendon-driven continuum manipulators," *IEEE Transactions on Robotics*, vol. 24, no. 6, pp. 1262–1273, 2008.

[5] I. Gravagne, C. Rahn, and I. Walker, "Large deflection dynamics and control for planar continuum robots," *IEEE/ASME Transactions on Mechatronics*, vol. 8, no. 2, pp. 299–307, 2003.

[6] J. Edelmann, A. Petruska, and B. Nelson, "Estimation-based control of a magnetic endoscope without device localization," *Journal of Medical Robotics Research*, vol. 3, no. 1, 2017.

[7] ——, "Magnetic control of continuum devices," *The International Journal of Robotics Research*, vol. 36, no. 1, pp. 68–85, 2017.

[8] M. Ikeuchi and K. Ikuta, "Development of pressure-driven micro active catheter using membrane micro emboss following excimer laser ablation (MeME-x) process," in *2009 IEEE International Conference on Robotics and Automation*. IEEE, may 2009.

[9] B. Jones and I. Walker, "Kinematics for multisection continuum robots," *IEEE Transactions on Robotics*, vol. 22, no. 1, pp. 43–55, feb 2006.

[10] ——, "Practical kinematics for real-time implementation of continuum robots," *IEEE Transactions on Robotics*, vol. 22, no. 6, pp. 1087–1099, dec 2006.

[11] M. Langelaar and F. Keulen, "Modeling of a shape memory alloy active catheter," *45th AIAA Structures, Structural Dynamics and Materials Conference*, pp. 19–22, 2004.

[12] S. Lee, S. Lee, H. An, S. Cha, J. Chang, B. Kim, and J. Pak, "Biomedical applications of electroactive polymers and shape memory alloys," *Proceedings of SPIE-The International Society for Optical Engineering*, vol. 4695, pp. 17–31, 2002.

[13] K. Lee, N. Munce, T. Shoa, L. Charron, G. Wright, J. Madden, and V. Yang, "Fabrication and characterization of laser-micromachined polypyrrole-based artificial muscle actuated catheters," *Sensors and Actuators A: Physical*, vol. 153, no. 2, pp. 230 – 236, 2009.

[14] K. Kim and S. Tadokoro, Eds., *Electroactive Polymers for Robotic Applications*. Springer London, 2007.

[15] P. Dupont, J. Lock, B. Itkowitz, and E. Butler, "Design and control of concentric-tube robots," *IEEE Transactions on Robotics*, vol. 26, no. 2, pp. 209–225, 2010.

[16] M. Chikhaoui, K. Rabenorosoa, and N. Andreff, "Kinematics and performance analysis of a novel concentric tube robotic structure with embedded soft micro-actuation," *Mechanism and Machine Theory*, vol. 104, pp. 234 – 254, 2016.

[17] J. Webster, J. Romano, and N. Cowan, "Mechanics of precurved-tube continuum robots," *IEEE Transactions on Robotics*, vol. 25, no. 1, pp. 67–78, 2009.

[18] N. Simaan, "Snake-like units using flexible backbones and actuation redundancy forenhanced miniaturization," in *Proceedings of the 2005 IEEE International Conference on Robotics and Automation (ICRA 2005)*, Barcelona, Spain, 2005, pp. 3012–3017.

[19] K. Xu and N. Simaan, "Analytic formulation for kinematics, statics and shape restoration of multibackbone continuum robots via elliptic integrals," *ASME Journal of Mechanisms and Robotics*, vol. 2, no. 1, pp. 011 006–1–011 006–13, 2010.

[20] L. Wang, G. Del Giudice, and N. Simaan, "Simplied kinematics of continuum robot equilibrium modulation via moment coupling effects and model calibration," *ASME Journal of Mechanisms and Robotics*, vol. 11, no. 5, 2019.

[21] C. Bryson and D. Rucker, "Toward parallel continuum manipulators," in *Proceedings of the 2014 IEEE International Conference on Robotics and Automation (ICRA 2014)*, 2014.

[22] C. Black, J. Till, and D. Rucker, "Parallel continuum robots: Modeling, analysis, and actuation-based force sensing," *IEEE Transactions on Robotics*, vol. 34, no. 1, pp. 29–47, 2017.

[23] O. Altuzarra, D. Caballero, F. Campa, and C. Pinto, "Forward and inverse kinematics in 2-dof planar parallel continuum manipulators," in *Proceedings of the European Conference on Mechanism Science (EuCoMeS 2018)*, Aachen, Germany, 2018.

[24] O. Altuzarra, D. Caballero, Q. Zhang, and F. Campa, "Kinematic characteristics of parallel continuum mechanisms," in *Proceedings of Advances in Robot Kinematics (ARK 2018)*, Bologna, Italy, 2018.

[25] O. Altuzarra and J. Merlet., "Certified kinematics solution of 2-dof planar parallel continuum mechanisms," in *Proceedings of the IFToMM World Congress on Mechanism and Machine Science*, Cracow, Poland, 2019, pp. 197–208.

[26] O. Altuzarra, D. Caballero, F. Campa, and C. Pinto, "Position analysis in planar parallel continuum mechanisms," *Mechanism and Machine Theory*, vol. 132, pp. 13–29, 2019.

[27] F. Campa, M. Diez, D. Diaz-Caneja, and O. Altuzarra, "A 2 dof continuum parallel robot for pick & place collaborative tasks," in *Advances in Mechanism and Machine Science*. Springer International Publishing, 2019, pp. 1979–1988.

[28] B. Mauze, R. Dahmouche, G. Laurent, N. Andreff, P. Rougeot, P. Sandoz, and C. Clevy, "Nanometer precision with a planar parallel continuum robot," *IEEE Robotics and Automation Letters*, vol. 5, no. 3, pp. 3806–3813, jul 2020.

[29] Z. Yang, X. Zhu, and K. Xu, "Continuum delta robot: a novel translational parallel robot with continuum joints," in *2018 IEEE/ASME International Conference on Advanced Intelligent Mechatronics (AIM)*. IEEE, jul 2018.

[30] P. Anderson, A. Mahoney, and R. Webster, "Continuum reconfigurable parallel robots for surgery: Shape sensing and state estimation with uncertainty," *IEEE Robotics and Automation Letters*, vol. 2, no. 3, pp. 1617–1624, jul 2017.

[31] A. Orekhov, C. Black, J. Till, S. Chung, and D. Rucker, "Analysis and validation of a teleoperated surgical parallel continuum manipulator," *IEEE Robotics and Automation Letters*, vol. 1, no. 2, pp. 828–835, jul 2016.

[32] J. Till and D. Rucker, "Elastic stability of Cosserat rods and parallel continuum robots," *IEEE Transactions on Robotics*, vol. 33, no. 3, pp. 718–733, 2017.

[33] J. Merlet, *Parallel Robots*, 2nd ed. Springer, 2006.

[34] C. Gosselin and J. Angeles, "Singularity analysis of closed-loop kinematic chains," *IEEE Transactions on Robotics and Automation*, vol. 6, no. 3, pp. 281–290, 1990.

[35] M. Conconi and M. Carricato, "A new assessment of singularities of parallel kinematic chains," *IEEE Transactions on Robotics*, vol. 25, no. 4, pp. 757–770, 2009.

[36] D. Zlatanov, R. Fenton, and B. Benhabib, "Singularity analysis of mechanisms and robots via a velocity-equation model of the instantaneous kinematics," in *Proceedings of the 1994 IEEE International Conference on Robotics and Automation (ICRA 1994)*, 1994.

[37] ——, "Singularity analysis of mechanisms and robots via a motion-space model of the instantaneous kinematics," in *Proceedings of the 1994 IEEE International Conference on Robotics and Automation (ICRA 1994*, 1994.

[38] D. Zlatanov, I. Bonev, and C. Gosselin, "Constraint singularities of parallel mechanisms," in *Proceedings 2002 IEEE International Conference on Robotics and Automation (ICRA 2002)*, vol. 1, Washington, DC, USA, 2002, pp. 496–502.

[39] S. Briot, G. Pagis, N. Bouton, and P. Martinet, "Degeneracy conditions of the dynamic model of parallel robots," *Multibody System Dynamics*, vol. 37, no. 4, pp. 371–412, 2016.

[40] J. Merlet, "Singular configurations of parallel manipulators and Grassmann geometry," *The International Journal of Robotics Research*, vol. 8, no. 5, pp. 45–56, 1989.

[41] D. Kanaan, P. Wenger, S. Caro, and D. Chablat, "Singularity analysis of lower mobility parallel manipulators using Grassmann–Cayley algebra," *IEEE Transactions on Robotics*, vol. 25, no. 5, pp. 995–1004, 995-1004.

[42] I. Bonev, D. Zlatanov, and C. Gosselin, "Singularity analysis of 3-dof planar parallel mechanisms via screw theory," *ASME Journal of Mechanical Design*, vol. 125, no. 3, pp. 573–581, 2003.

[43] J. Merlet, "Interval analysis and robotics," in *Principles and Practice of Constraint Programming - CP 2006*. Springer Berlin Heidelberg, 2006.

[44] Y. Ganji and F. Janabi-Sharifi, "Catheter Kinematics for Intracardiac Navigation," *IEEE Transactions on Biomedical Engineering*, vol. 56, no. 3, pp. 621–632, Mar. 2009.

[45] A. Mayer and O. Sawodny, "Singularity and workspace analysis for modular continuum robots," in *2018 IEEE Conference on Control Technology and Applications (CCTA)*. IEEE, aug 2018.

[46] O. Altuzarra and F. J. Campa, "On singularity and instability in a planar parallel continuum mechanism," in *Advances in Robot Kinematics 2020*, J. Lenarčič and B. Siciliano, Eds. Cham: Springer International Publishing, 2021, pp. 327–334.

[47] C. Quennouelle and C. Gosselin, "Kinematostatic modeling of compliant parallel mechanisms," *Meccanica*, vol. 46, no. 1, pp. 155–169, jan 2011.

[48] F. Zaccaria, S. Briot, M. Chikhaoui, E. Idà, and M. Carricato, "An analytical formulation for the geometrico-static problem of continuum planar parallel robots," in *Proceedings of the 23rd CISM IFToMM Symposium on Robot Design, Dynamics and Control (RoManSy 2020)*, 2020.

[49] A. Lazarus, J. Miller, and P. Reis, "Continuation of equilibria and stability of slender elasticrods using an asymptotic numerical method," *Journal of the Mechanics and Physics of Solids*, vol. 61, no. 8, pp. 1712–1736, 2013.

[50] Q. Peyron, K. Rabenorosoa, N. Andreff, and P. Renaud, "A numerical framework for the stability and cardinality analysis of concentric tube robots: Introduction and application to the follow-the-leader deployment," *Mechanism and Machine Theory*, vol. 132, pp. 176–192, 2019.

[51] H. Ziegler, *Principles of Structural Stability*. Cambridge, MA, USA: Birkhäuser, 1977.

[52] A. Garriga-Casanovas and F. Rodriguez y Baena, "Kinematics of continuum robots with constant curvature bendingand extension capabilities," *ASME Journal of Mechanisms and Robotics*, vol. 11, no. 1, pp. 011 010–1–011 010–12, 2019.

[53] D. Rucker and R. Webster, "Computing jacobians and compliance matrices for externally loaded continuum robots," in *Proceedings of the 2011 IEEE International Conference on Robotics and Automation (ICRA 2011)*, 2011, pp. 945–950.

[54] F. Armero and J. Valverde, "Invariant hermitian finite elements for thin kirchhoff rods. i: The linear plane case," *Computer Methods in Applied Mechanics and Engineering*, vol. 213-216, pp. 427 – 457, 2012.

[55] F. Boyer and D. Primault, "Finite element of slender beams in finite transformations: a geometrically exact approach," *International Journal for Numerical Methods in Engineering*, vol. 59, pp. 669–702, 2004.

[56] F. Boyer, V. Lebastard, F. Candelier, and F. Renda, "Dynamics of continuum and soft robots: A strain parameterization based approach," *IEEE Transactions on Robotics*, 2020.

[57] H. Qin and D. Terzopoulos, "D-NURBS: A physics-based framework for geometric design," *IEEE Transactions on Visualization and Computer Graphics*, vol. 2, no. 1, pp. 85–96, 1996.

[58] S. Briot and A. Goldsztejn, "Technical report associated with the paper "Singularity Conditions for Continuum Parallel Robots"," CNRS, Laboratoire des Sciences du Numérique de Nantes (LS2N), Tech. Rep., 2020. [Online]. Available: https://hal.archives-ouvertes.fr/hal-03210572

[59] F. Renda, M. Giorelli, M. Calisti, M. Cianchetti, and C. Laschi, "Dynamic model of a multibending soft robot arm driven by cables," *IEEE Transactions on Robotics*, vol. 30, no. 5, pp. 1109–1122, 2014.

[60] D. Rucker and R. Webster III, "Statics and dynamics of continuum robots with general tendon routing and external loading," *IEEE Transactions on Robotics*, vol. 27, no. 6, pp. 1033–1044, 2011.

[61] Q. Peyron, Q. Boehler, K. Rabenorosoa, B. Nelson, P. Renaud, and N. Andreff, "Kinematic analysis of magnetic continuum robots using continuation method and bifurcation analysis," *IEEE Robotics and Automation Letters*, vol. 3, no. 4, pp. 3646–3653, 2018.

[62] H. Lang, J. Linn, and M. Arnold, "Multi-body dynamics simulation of geometrically exact cosserat rods," *Multibody System Dynamics*, vol. 25, no. 3, pp. 285–312, 2010.

[63] J. Burgess, "Bending stiffness in a simulation of undersea cable deployment," *International Journal of Offshore and Polar Engineering*, vol. 3, no. 3, pp. 197–204, 1993.

[64] C. Gatti-Bono and N. Perkins, "Physical numerical modelling of the dynamic behavior of fly line," *Journal of Sound and Vibration*, vol. 255, no. 3, pp. 555–577, 2002.

[65] J. Spillmann and M. Teschner, "CORDE: Cosserat rod elements for the dynamic simulation of one-dimensional elastic objects," *Eurographics/ACM SIGGRAPH*, pp. 63–72, 08 2007.

[66] P. Jung, S. Leyendecker, J. Linn, and M. Ortiz, "A discrete mechanics approach to the Cosserat rod theory – Part 1: static equilibria," *International Journal for Numerical Methods in Engeneering*, vol. 85, no. 1, 2010.

[67] J. Nocedal and S. Wright, *Numerical Optimization*, 2nd ed. Springer, 2006.

[68] K. Hunt, *Kinematic geometry of mechanisms*. Oxford: Clarendon Press, 1978.

[69] A. Goldsztejn and L. Granvilliers, "A New Framework for Sharp and Efficient Resolution of NCSP with Manifolds of Solutions," *Constraints*, vol. 15, no. 2, pp. 190–212, 2010.

[70] B. Martin, A. Goldsztejn, C. Jermann, and L. Granvilliers, "Certified Parallelotope Continuation for One-Manifolds," *SIAM Journal On Numerical Analysis*, vol. 51, no. 6, pp. 3373–3401, 2013.

[71] S. Caro, D. Chablat, A. Goldsztejn, D. Ishii, and C. Jermann, "A Branch and Prune Algorithm for the Computation of Generalized Aspects of Parallel Robots," *Artificial Intelligence*, vol. 221, pp. 34–50, 2014.

[72] M. Zein, P. Wenger, and D. Chablat, "Non-singular assembly-mode changing motions for 3-RPR parallel manipulators," *Mechanism and Machine Theory*, vol. 43, no. 4, pp. 480–490, 2008.

[73] J. Merlet, "Jacobian, manipulability, condition number, and accuracy of parallel robots," *ASME Journal of Mechanical Design*, vol. 128, no. 1, pp. 199–206, 2006.

Sébastien Briot received the B.S. and M.S. degrees in mechanical engineering in 2004 and the Ph.D. degree in robotics (under the supervision of Prof. V. Arakelian) in 2007, from the Institut National des Sciences Appliquées de Rennes, Rennes, France. He was a Postdoctoral Fellow with the Ecole de Technologie Supérieure, Montreal, QC, Canada, in 2008. Since 2009, he has been a full-time CNRS Researcher with the Laboratoire des Sciences du Numérique de Nantes, Nantes, France, where he has been the Head of the ARMEN Research Team since 2017. He has authored 45 referred journal papers, two books, and three inventions. His research interests include the design optimization of robots and the analysis of their performance, especially their singularities. Dr. Briot received the Best Ph.D. Thesis Award in Robotics from the French CNRS in 2007. In 2011, he received two other awards: the Award for the Best Young Researcher from the French Region Bretagne and the Award for the Best Young Researcher from the French Section of the American Society of Mechanical Engineering.

Alexandre Goldsztejn received his engineer degree from the Institut Supérieur d'Electronique et du Numérique, Lille, France, in 2001, and his Ph.D. in Computer Science from the University of Nice-Sophia Antipolis in 2005. He has spent one year as a postdoctoral fellow in the University of Central Arkansas and the University of California Irvine. He is full time CNRS researcher since 2007.

His research interests include interval analysis and its application to constraint satisfaction, nonlinear global optimization, robotics and control.